JGR Earth Surface

RESEARCH ARTICLE
10.1029/2023JF007164

Cosmogenic Nuclide Tracking of Sediment Recycling From a Frontal Siwalik Range in the Northwestern Himalaya

Sanjay Kumar Mandal[1,2], René Kapannusch[3], Dirk Scherler[3,4], Jason B. Barnes[5], Nadja Insel[6], and Alexander L. Densmore[7]

[1]Department of Earth Sciences, Indian Institute of Science Education and Research Kolkata, Nadia, India, [2]Centre for Climate and Environmental Studies, Indian Institute of Science Education and Research Kolkata, Nadia, India, [3]Earth Surface Geochemistry, GFZ German Research Centre for Geosciences, Potsdam, Germany, [4]Institute of Geographical Sciences, Freie Universität Berlin, Berlin, Germany, [5]Landscape Analytics LLC, Seattle, WA, USA, [6]Department of Earth Science, Northeastern Illinois University, Chicago, IL, USA, [7]Department of Geography, Institute of Hazard, Risk, and Resilience, Durham University, Durham, UK

Abstract The Himalayan orogen exports millions of tons of sediment annually to the Indo-Gangetic foreland basin, derived from both hinterland and foreland fold-thrust belts (FTB). Although erosion rates in the hinterland are well-constrained, erosion rates in the foreland FTB and, by extension, the sediment flux have remained poorly constrained. Here, we quantified erosion rates and sediment flux from the Mohand Range in the northwestern Himalaya by modeling and measuring the cosmogenic radionuclide (CRN) ^{10}Be and ^{26}Al concentrations in modern fluvial sediments. Our model uses local geological and geophysical constraints and accounts for CRN inheritance and sediment recycling, which enables us to determine the relative contributions of the hinterland and foreland FTB sources to the CRN budget of the proximal foreland deposits. Our model predictions closely match measured concentrations for a crustal shortening rate across the Mohand Range of 8.0 ± 0.5 mm yr^{-1} (i.e., approximately 50% of the total shortening across the Himalaya at this longitude) since $0.75^{+0.02}_{-0.06}$ Ma. This shortening implies a spatial gradient in erosion rates ranging from 0.42 ± 0.03 to 4.92 ± 0.34 mm yr^{-1}, controlled by the geometry of the underlying structure. This erosion pattern corresponds to an annual sediment recycling of ∼2.0 megatons from the Mohand Range to the downstream Yamuna foreland. Converted to sediment fluxes per unit width along the Himalaya, the foreland FTB accounts for ∼21% ± 5% of the total flux entering the foreland. Because these sediments have lower ^{10}Be concentrations than hinterland-derived sediment, they would lead to ∼14% overestimation of ^{10}Be-derived erosion rates, based on Yamuna sediments in the proximal foreland.

Plain Language Summary Cosmogenic radionuclides such as beryllium-10 (^{10}Be) are important tools for tracking erosion processes at the Earth's surface. However, they are challenging to apply when sediment remains temporarily stored for millions of years before being re-eroded. We call this sediment recycling. We quantified sediment recycling in the Mohand Range, at the foothills of the northwestern Himalaya, based on the present-day ^{10}Be concentration in fluvial sediments recycled from tectonically uplifted older foreland deposits. We do this by modeling how the ^{10}Be concentrations change as sediment is first eroded in the Himalayan source region, then deposited in the foreland, and finally eroded again. By comparing modeled and measured concentrations, we find that erosion rates in the Mohand Range vary from 0.42 ± 0.03 to 4.92 ± 0.34 mm yr^{-1}, corresponding to about 2.0 megatons of sediment recycling from this range to the downstream Yamuna foreland. Because the ^{10}Be concentration in recycled sediment is lower than that in sediment eroded from the high Himalaya, admixing high Himalayan sediments with recycled material may result in erosion rates that are higher than the actual erosion rates in the high Himalaya.

Key Points:

- Novel approach for tracking cosmogenic nuclide accumulation in fluvial sediments through each step of a fold-thrust belt sediment routing system
- ^{10}Be-derived erosion rates and sediment flux from the Mohand Range in the northwestern Himalaya
- Onset of Main Frontal Thrust motion and rate of crustal shortening across the Mohand Range constrained by modeling ^{10}Be concentrations in present-day river sediments

Supporting Information:

Supporting Information may be found in the online version of this article.

Correspondence to:

S. K. Mandal,
sanjaykm@iiserkol.ac.in

Citation:

Mandal, S. K., Kapannusch, R., Scherler, D., Barnes, J. B., Insel, N., & Densmore, A. L. (2023). Cosmogenic nuclide tracking of sediment recycling from a Frontal Siwalik range in the northwestern Himalaya. *Journal of Geophysical Research: Earth Surface*, *128*, e2023JF007164. https://doi.org/10.1029/2023JF007164

Received 10 MAR 2023
Accepted 9 NOV 2023

Author Contributions:

Conceptualization: Sanjay Kumar Mandal, Dirk Scherler
Data curation: René Kapannusch, Jason B. Barnes, Nadja Insel
Formal analysis: Sanjay Kumar Mandal, Dirk Scherler
Funding acquisition: Sanjay Kumar Mandal, Dirk Scherler, Jason B. Barnes, Alexander L. Densmore
Investigation: Sanjay Kumar Mandal, Dirk Scherler

1. Introduction

The Indian and Eurasian plates have been colliding since ∼54 Ma (Najman et al., 2017), forming the ∼2,500-km long Himalaya south of the Tibetan Plateau (Figure 1a). Annually, Himalayan erosion supplies millions of tons of sediment and solutes to the Indo-Gangetic foreland basin and, eventually, to the ocean (e.g., Milliman & Farnsworth, 2011). This enormous sediment discharge includes material eroded from the internal part of the orogen (referred to as the hinterland), which consists of stacked and basal-accreted thrust sheets (e.g., P. Srivastava & Mitra, 1994), as well as material eroded from the outboard fold-thrust belts (referred to as the foreland FTB),

Methodology: Sanjay Kumar Mandal, René Kapannusch, Dirk Scherler
Resources: Alexander L. Densmore
Software: Sanjay Kumar Mandal, René Kapannusch, Dirk Scherler
Validation: Sanjay Kumar Mandal, Dirk Scherler
Visualization: Sanjay Kumar Mandal
Writing – original draft: Sanjay Kumar Mandal
Writing – review & editing: Sanjay Kumar Mandal, Dirk Scherler, Jason B. Barnes, Alexander L. Densmore

which consists of deformed older foreland basin successions (Figure 1b) (e.g., Najman et al., 2004; Powers et al., 1998). The determination of sediment fluxes from these two source regions is the key physical measure that enables us to constrain processes such as orogenic sediment recycling, chemical weathering, and organic carbon fluxes (e.g., Galy et al., 2007; Lupker et al., 2012, 2013), which in turn, leads to an improved understanding of the long-term links between climate, tectonics, and surface processes.

The estimation of sediment flux from Himalayan river catchments over timescales ranging from 10^1 to 10^4 years is primarily reliant on sediment gauging (e.g., Andermann et al., 2012; Gabet et al., 2008) and analyses of cosmogenic radionuclides (CRN) such as ^{10}Be (e.g., Vance et al., 2003). Under the assumption of steady-state erosion, the ^{10}Be concentrations measured in fluvial sediments provide an estimate

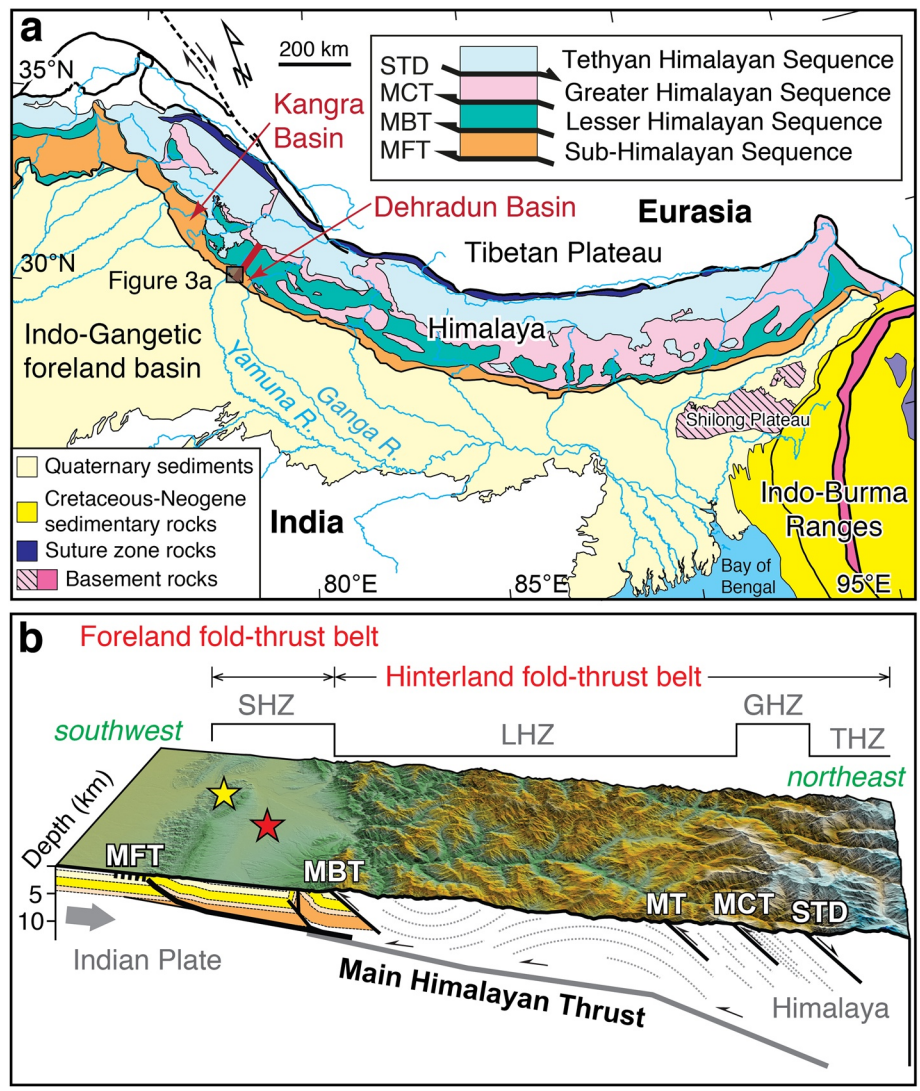

Figure 1. Geology of the Himalaya. (a) Regional geology of the Himalayan orogen and its Indo-Gangetic foreland (modified from Webb et al. (2011)). Thick red line is the line of section in panel (b). STD = South Tibetan Detachment; MCT = Main Central Thrust; MBT = Main Boundary Thrust; and MFT = Main Frontal Thrust. (b) Perspective view of topography and structure across the northwestern Himalaya. Yellow and red stars indicate the Mohand Range and Dehradun Basin, respectively. MT = Munsiari Thrust. The depth of the Main Himalayan Thrust between the MFT and MBT is based on seismic reflection profiles across the Dehradun Basin (Powers et al., 1998) and at distances >70 km from the mountain front is based on teleseismic receiver-function studies along the Alaknanda River ~100 km further southeast (Caldwell et al., 2013). The subsurface structure beneath the foreland fold-thrust belt is based on the balanced cross-section across the Dehradun Basin after Mishra and Mukhopadhyay (2002). SHZ = Sub-Himalayan Zone; LHZ = Lesser Himalayan Zone; GHZ = Greater Himalayan Zone; and THZ = Tethyan Himalayan Zone.

of catchment-averaged erosion rates (Bierman & Steig, 1996; Brown et al., 1995; Granger et al., 1996). Such catchment-wide erosion rates enable constraining orogenic sediment flux over intermediate timescales (10^2–10^3 yr) and spatial scales spanning from individual Himalayan river catchments to the whole mountain range (Dingle et al., 2018; Lupker et al., 2012; Scherler et al., 2014). However, erosion rates and sediment fluxes of the foreland FTBs, which consist of arrays of km-scale folds, remain poorly constrained. This shortcoming is due in part to challenges in estimating catchment-wide erosion rates using the concentration of ^{10}Be measured in detrital quartz grains recycled from the older foreland successions. The sediment pathway from hinterland to foreland is complex and multi-step as follows: (1) sediment creation via hinterland erosion, (2) transport from hinterland to foreland, (3, 4) burial and storage within the sedimentary basin, and (5) later uplift via thrusting and folding, which makes sediment available for re-exhumation (recycling) (Figure 2) (e.g., Charreau et al., 2011, 2020; Mandal et al., 2021). As a consequence, the recycled quartz grains contain nuclides acquired during prior exposure (steps 1–4), resulting in inheritance and, as a result, anomalously low erosion rates. Therefore, to estimate erosion rates using present-day ^{10}Be concentrations in fluvial sediments, we must be able to separate the number of ^{10}Be atoms (per gram of quartz) gained during recycling (step 5) from the inheritance. Although a few studies have attempted to reconstruct hinterland paleoerosion rates using present-day ^{10}Be concentrations in tectonically uplifted late Miocene-Pleistocene foreland basin deposits (Charreau et al., 2020; Mandal et al., 2021), this challenge has yet to be explored and applied to a regional case study.

Here, we present a novel approach for quantifying erosion rates of foreland FTBs by comparing measured and modeled CRN concentrations in fluvial sediments. We apply this approach to the Mohand Range, an emergent fault-related fold in the frontal part of the northwestern Himalaya (Figure 3). This range is particularly suitable for this approach for several reasons. First, provenance studies have constrained the sediment source region (Kumar et al., 2003; Mandal et al., 2018). Second, paleomagnetic studies constrained the timing and rate of sediment deposition in the foreland basin (Sangode et al., 1996, 1999). Third, ^{10}Be studies quantified the past

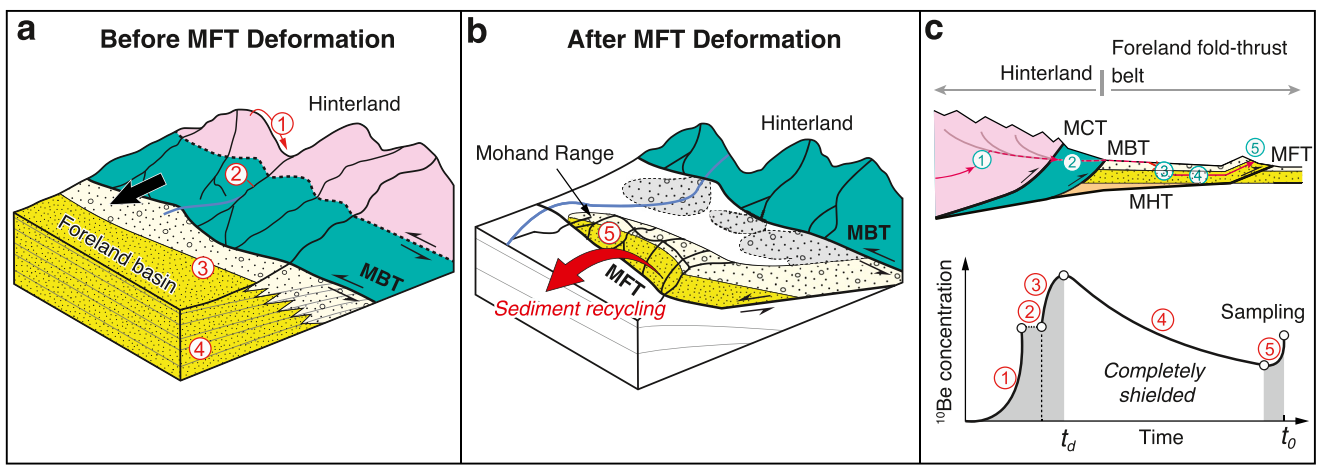

Figure 2. Pathway of uplifted older foreland deposits in the Himalayan foreland fold-thrust belt and the conceptual evolution of cosmogenic radionuclide (CRN) accumulation in uplifted foreland deposits. Generalized pathway of sediments (modified from Densmore et al. (2015)) as follows: (a) Step 1: Source region erosion generates an initial CRN concentration (N_E). Step 2: Sediment transport from hinterland source region to the foreland via a large river system. It is assumed that the short sediment transit time caused negligible nuclide accumulation (N_T) during this step (see Section 3.1). Step 3: Sediment is deposited and buried gradually in the foreland basin, causing additional CRN accumulation (N_B). Step 4: Deeply buried sediments lose CRNs due to radioactive decay. (b) Step 5: Thin-skinned tectonics causes foreland accretion at the mountain front and generates uplift of the buried foreland strata. Eventually, erosion re-exposes uplifted sedimentary rocks to cosmic rays, thereby accumulating more CRNs (N_X). (c) Schematic evolution of CRNs in thrusted foreland material during their journey through steps 1–5 shown in panels (a, b). Concentrations increase (gray areas) and decrease (white area) during different times as sediment is eroded, deposited, buried, and recycled (modified after Charreau et al. (2011)). t_d = time of sediment deposition; t_0 = time of the CRN analysis.

and present-day erosion rates in the hinterland source regions (Mandal et al., 2021; Scherler et al., 2014). Fourth, geophysical data constrain the décollement geometry, which is the dominant cause for spatial variations in uplift rate across the range (Powers et al., 1998). Fifth, structural geological studies constrained the growth model of this range and associated crustal shortening (Mishra & Mukhopadhyay, 2002; Powers et al., 1998; V. Srivastava et al., 2018). These constraints allowed us to simulate present-day surface CRN concentrations across the Mohand Range resulting from the entire sedimentary pathway since erosion in the hinterland (steps 1–5 in Figure 2). By calibrating our model using a set of ^{10}Be and ^{26}Al concentrations measured in fluvial sediments, we quantify regional-scale modern erosion rates and, thus, the recycled sediment discharge from the Mohand Range into the adjacent foreland. Furthermore, our approach provides additional independent constraints on the onset of fold growth and the concomitant crustal shortening rate absorbed by the deformed foreland succession in the Mohand Range. In the following, we present (a) a ^{10}Be data set measured in 23 fluvial sediments and two bedrock samples, (b) a ^{26}Al-^{10}Be pair data set measured in an additional 10 fluvial sediment samples, (c) model predictions of ^{10}Be and ^{26}Al concentrations in our analyzed samples, and (d) a comparison between simulations and observations. Finally, we discuss the limitations of our approach and its implication for estimating the shortening rate and recycled sediment flux into the proximal Himalayan foreland.

2. Background

2.1. Geologic and Geomorphic Setting

Crustal shortening associated with Cenozoic Himalayan mountain building resulted in an FTB and foreland basin system. The FTB in the northwestern Himalaya is a southward-tapering orogenic wedge composed of Paleoproterozoic to Neogene rocks carried southward relative to northward underthrusting of India (Figure 1) (Webb et al., 2011; Yin & Harrison, 2000). The major thrust faults are interpreted to splay from the Main Himalayan Thrust (MHT, Figure 1b), the basal décollement along which the Indian Plate thrusts beneath the Himalaya (Avouac, 2015). The thrust belt strikes northwest-southeast, verges southwestward, and divides the orogen into four major tectonostratigraphic zones. From north to south, these zones are (a) the Tethyan Himalaya of Ordovician-Cretaceous metasedimentary and sedimentary rocks, (b) the Greater Himalaya of high-grade metamorphic rocks, (c) the Lesser Himalaya of Paleoproterozoic-Cambrian metasedimentary rocks with sparse exposures of younger Phanerozoic rocks, and (d) the Sub-Himalaya of folded and thrusted Cenozoic foreland deposits (Figure 3) (Hodges, 2000). The Main Boundary Thrust (MBT) separates the Sub-Himalaya in the footwall from the Lesser Himalaya in the hanging wall, whereas the Main Central Thrust (MCT) separates the Lesser Himalaya from both the Greater and Tethyan Himalaya in the MCT hanging wall (Figure 3a) (P. Srivastava & Mitra, 1994; Webb et al., 2011).

The Cenozoic foreland deposits comprise Eocene to early Miocene limestone, shale, sandstone, and minor conglomerate of the Subathu and Dharamsala Formations, followed by middle Miocene-Pleistocene mudstone, siltstone, sandstone, and conglomerate of the Siwalik Group (Figure 3b) (Najman et al., 2004). The Siwalik Group is informally divided into lower, middle, and upper formations. The frontal Sub-Himalaya is composed of thrust sheets of the Siwalik Group carried by the Main Frontal Thrust (MFT) system (Figure 3c) (Mishra & Mukhopadhyay, 2002; Powers et al., 1998), which is the youngest, most active, and southernmost thrust system in the Himalaya (Avouac, 2015). Stratigraphic sections, surface dips of deformed Siwalik strata, and sparse reflection seismic data have demonstrated that faults carrying these thrust sheets branch upward from the MHT décollement (Mishra & Mukhopadhyay, 2002; Powers et al., 1998). Thin-skinned tectonics deformed the Siwalik stratigraphy and created both a wedge-top basin (hereafter Dehradun Basin) and parallel rows of northwest-southeast striking folds (Figure 3b). After leaving the high mountain (hinterland) and before entering the alluvial piedmont (i.e., the proximal foredeep depozone in the footwall of the MFT), the southward-flowing main rivers, that is, Yamuna and Ganga rivers, traverse the lateral margins of the Dehradun Basin.

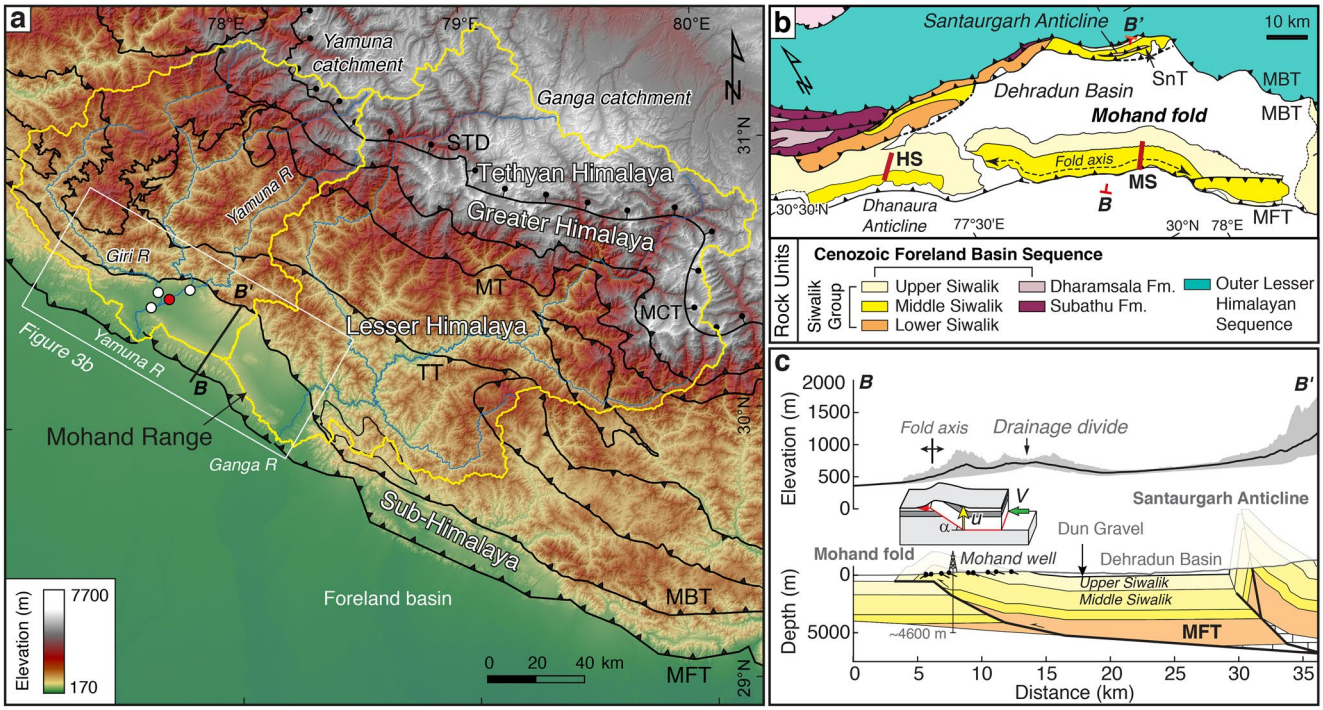

Figure 3. Tectonomorphology of the northwestern Himalaya. (a) ALOS World 3D-30 m digital elevation model of the Ganga and Yamuna catchments and Dehradun Basin. TT = Tons Thrust. White circles are sample locations of modern hinterland-derived sediment analyzed for ^{10}Be by Mandal et al. (2021) and red circle shows location of sample analyzed for ^{10}Be by Lupker et al. (2012). B-B' = location of the balanced structural cross section shown in panel (c). (b) Geology of the foreland fold-thrust belt in the study area (modified after Mishra and Mukhopadhyay (2002), Kumar et al. (2003), and Thakur et al. (2007)). Thick red lines represent the locations of magnetostratigraphic sections of the Siwalik Group (HS = Haripur section (Sangode et al., 1996) and MS = Mohand section (Sangode et al., 1999)). SnT = Santaurgarh Thrust. (c) 13 km wide swath-averaged minimum, mean, and maximum elevation profiles above the balanced cross section (modified from Mishra and Mukhopadhyay (2002)). Inset shows relationship between the rock uplift rate (u) and horizontal shortening rate (V) assuming fault-bend folding of Siwalik strata above the Main Frontal Thrust.

2.2. The Mohand Range

The northwest-southeast trending Mohand Range defines the deformation front and exposes Siwalik Group rocks uplifted over a ramp in the MFT (Figure 3c). The range measures ~80 km along strike, has a width of ~15 km, and ~500 m of total relief, and is widely considered to be a fault-related anticline, constrained by geological, geophysical, and drill-core data (e.g., Mishra & Mukhopadhyay, 2002; Powers et al., 1998; Wesnousky et al., 1999). However, recent studies have attributed this range to a fault-related monocline (V. Srivastava et al., 2018). Magneto-stratigraphic studies constrain the chronology of stratigraphic accumulation between ca. 10 and <0.7 Ma (Sangode et al., 1996, 1999). The Dun Gravel unconformably overlies the Upper Siwalik units exposed along the northern range flank (Figure 4a) (Thakur et al., 2007). Based on the magnetostratigraphy of the Siwalik section in the nearby MFT-related fold (Figure 3b), previous studies have conjectured the onset of range growth to <0.773 Ma (Barnes et al., 2011; Thakur et al., 2007). Restoration of structural cross-sections yields 4–9 km of shortening of the Siwalik rocks across the Mohand Range (Mishra & Mukhopadhyay, 2002; Powers et al., 1998; V. Srivastava et al., 2018).

The Yamuna and Ganga Rivers traverse the western and eastern ends of the Mohand Range before entering the Gangetic Plain (Figure 3a). The range itself displays an asymmetric drainage pattern, with larger catchments on the steep southern flank feeding directly into the Gangetic Plain, compared to small and narrowly spaced catchments on the northern flank feeding into the Dehradun Basin (Figure 4). This asymmetry is thought to be controlled by the interplay between the across-strike rock uplift pattern, controlled by the MFT geometry, and the contrasting base levels (Barnes et al., 2011). Rivers south of the drainage divide traverse higher uplift rates as they flow downstream through the Upper Siwalik conglomerates, across a conglomerate-sandstone transitional zone, and then across poorly indurated sandstone-dominated Middle Siwaliks before debouching into the Gangetic Plain. Rivers north of the divide traverse lower uplift rates as they flow through the Upper Siwalik conglomerates near their headwaters and the Dun Gravel farther downstream (Figure 4a). The Asan and Suswa-Song Rivers set the base level for north-draining rivers, whereas the Gangetic Plain sets the base level for south-draining rivers (Figure 4a). The drainage divide reaches ~800–900 m

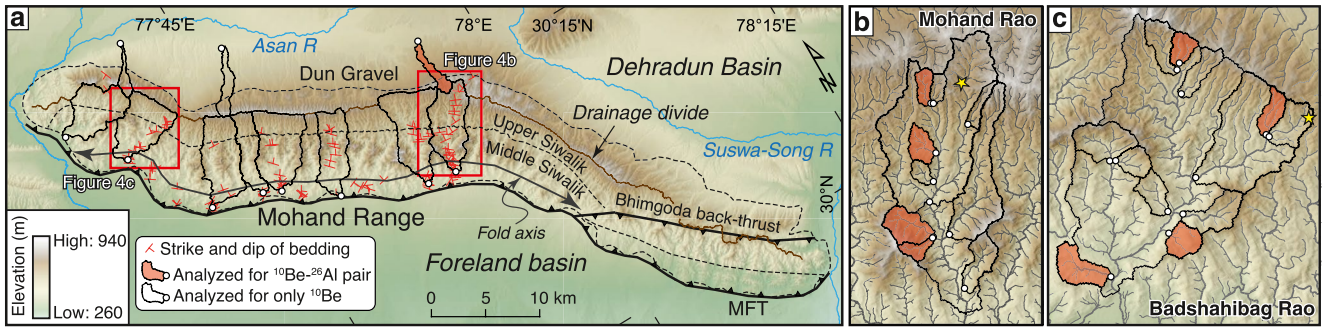

Figure 4. Topography of the Mohand Range and catchments sampled in this study. (a) ALOS World 3D-30 m digital elevation model of the Mohand Range, ^{10}Be-^{26}Al sample locations and associated drainage basins, drainage divide, and fold axis (after Mishra and Mukhopadhyay (2002)). Strike and dip of the bedding after V. Srivastava et al. (2018). (b, c) Sampled sub-catchments of the Mohand Rao and Badshahibag Rao basins, respectively. Yellow stars are locations of bedrock samples analyzed for ^{10}Be.

above sea level and is located near the Upper Siwalik-Dun Gravel contact. So far, erosion by the south-draining rivers has exposed a >2 km thick Siwalik succession across the Mohand Range. Despite the Pleistocene age of the Mohand Range, the topography, high inferred rates of rock uplift and erosion, and substantial erosion since folding began all suggest that the range is in a topographic steady state (Allen et al., 2013; Barnes et al., 2011; Kirby & Whipple, 2012).

2.3. Sediment Provenance

To determine ^{10}Be concentrations inherited from paleoerosion, knowledge of sediment source areas is required (see Section 3.1). The underthrusting of the Indian Plate beneath South Tibet and concomitant crustal shortening implies that over the past several million years, the Himalayan mountain front has migrated toward the south (Lyon-Caen & Molnar, 1985; Mugnier & Huyghe, 2006). This is supported by the upward coarsening of the Siwalik succession in the Mohand Range, where medium- to coarse-grained sandstones of the Middle Siwalik Formation grade into pebble- and cobble-sized conglomerates of the Upper Siwalik Formation. Assuming a steady convergence rate of ~18 mm yr^{-1} (Stevens & Avouac, 2015) and that two-thirds of this is accommodated by underthrusting (Avouac, 2015), 10-Myr old Siwalik sediments were deposited ~120 km downstream from their present location. Analogous to the modern drainage pattern of the Gangetic Plain, deposition at such a distal foreland basin location was likely dominated by the Yamuna or Ganga River. This inference is consistent with the deposition of thick multistory sandstone complexes during the late Miocene by south- to southeasterly flowing meandering to braided river systems (Kumar et al., 2004), which is analogous to the Pleistocene-Holocene Yamuna deposits in the Gangetic Plain (van Dijk et al., 2016). As the thrust front advanced further into the foreland basin, the depocenter transitioned to a gravelly proximal fan setting, consistent with the deposition of thick conglomerates. The predominance of quartzite (60%–80%) and subordinate crystalline (granite and gneiss) pebbles in the Upper Siwalik conglomerates suggests that sediments sourced from the inner Lesser and Greater Himalayan units (Kumar et al., 2003). Comparison of Sr and Nd isotopic and U-Pb geochronological data of Siwalik sandstones, sampled from the Mohand and Haripur sections in the Dehradun Basin, with possible source areas surrounding the Dehradun Basin led Mandal et al. (2018) to conclude that the uplifted Siwalik sediments in the western Mohand Range originated from the Yamuna catchment.

3. Methods

3.1. CRN Accumulation in Foreland Sediments

The cumulative concentration of in situ-produced CRN in sediment recycled from an uplifted foreland succession (N) consists of concentrations acquired during paleoerosion in the hinterland (N_E), transport to the foreland (N_T), deposition and burial in the foreland (N_B), adjusted for radioactive decay losses, and augmented by renewed accumulation resulting from erosion of the uplifting foreland succession (N_X) (Figure 2; steps 1–5) (e.g., Charreau et al., 2011; Mandal et al., 2021). Before reaching the foreland, sediments may be stored in intermontane valleys at the rapidly eroding front of the Himalaya for a considerable period. However, a compilation of the ages of currently exposed valley fills straddling major transverse drainages in the northwestern Himalaya (Scherler et al., 2015) shows that temporary sediment storage, before being re-entrained and flushed downstream to the foreland, seldom exceeds 50 kyr. Such short storage times are expected due to the high erosion rates in the Himalaya. For context, 50 kyr of intermontane sediment

storage corresponds to <2.5% decay of the existing cosmogenic ^{10}Be in hinterland-derived sediment prior to deposition in the foreland basin. Furthermore, additional accumulation of ^{10}Be during transient storage is limited to the thin uppermost layer of valley fill and is, therefore, expected to be volumetrically tiny (Scherler et al., 2014).

As the older foreland sediment was deposited tens of kilometers away from the mountain front (Section 2.3), the sediment transfer through the floodplain may cause an additional change in hinterland sediment CRN concentration (e.g., Ben-Israel et al., 2022). However, the study by Lupker et al. (2012) demonstrates that 1,000 km of sediment transfer through the Gangetic Plain would only enhance the initial ^{10}Be concentration in Himalayan sediment by about 13%. The ca. 120 km floodplain transfer distance (see Section 2.3) of the older (ca. 10 Ma) Mohand sediment is relatively short, and thus we expect no significant source of CRN build-up, consistent with ^{10}Be data from the Amazon foreland basin (e.g., Wittmann et al., 2009). We, therefore, assume that the CRN production during source-to-sink sediment transfer (i.e., N_T) is negligible. Hence, the present-day ^{10}Be concentration (N) in sediment eroded from the uplifted Siwalik succession can be described as:

$$N = \underbrace{(N_E + N_B)e^{-\lambda t_d}}_{N_{inh}} + N_X \quad (1)$$

where t_d is the time when sediments were deposited in the foreland basin and λ is the ^{10}Be decay constant (yr^{-1}). For discussion purposes, we define paleoerosion (N_E) and burial (N_B) contributions as inherited components (N_{inh}) because these precede nuclide accumulation added during Siwalik uplift and erosion.

The presence of inheritance precludes direct quantification of millennial-scale erosion rates of Mohand Range river catchments using CRNs. Instead, we propose combining existing geological, geophysical, and geochemical constraints with a model to predict the present-day CRN concentrations in surface sediments by sequentially estimating each component (N_E, N_B, and N_X) on the right side of Equation 1, and comparing the modeled concentrations and measured concentrations (N) to estimate the model parameters. To do this, we analyzed ^{10}Be in 23 fluvial sediment samples and two bedrock samples. We also analyzed ^{26}Al-^{10}Be pairs in 10 additional fluvial sediment samples collected from the western Mohand Range. We then simulated the spatial distribution of ^{10}Be and ^{26}Al concentrations across this range using the fundamental physical laws of CRN production and decay in conjunction with geological constraints on the history of past erosion and burial of uplifted older foreland sediments. The following sections describe the analytical procedures and the modeling of the spatial distribution of CRN concentrations and erosion rates across the Mohand Range. Finally, based on the observations reviewed in Section 2, we describe how the existing geological data enabled us to constrain the model.

3.2. Cosmogenic ^{10}Be and ^{26}Al Analyses

We collected sediment samples from ephemeral rivers during the low-flow season (September and January), when the entire channel bed was accessible. We collected sediment from several sand-gravel bars within and along the margins of channels to increase the probability that each sample is a representative amalgam of particles generated across the entire catchment. Eleven samples were collected from catchments draining the northern and southern flanks of the Mohand Range (Figure 4a). Since these samples represent an amalgam of sediments eroded from the Siwalik successions with a wide range of depositional ages (see Section 2.2), we also collected samples from 22 sub-catchments in the Mohand Rao and Badshahibag Rao drainage basins. These samples each cover a narrower depositional age range. In addition to these sediment samples, we collected two sandstone samples from the headwater regions of the Mohand Rao and Badshahibag Rao basins (Figures 4b and 4c).

We conducted quartz isolation and Be and Al extraction on the 250–1,000 μm size fraction of sediment and crushed bedrock samples at the PRIME Lab, Purdue University (sample name prefix "JB"; Dataset S1) and at the Helmholtz Laboratory for the Geochemistry of the Earth Surface (HELGES) at GFZ Potsdam (sample name prefix "RK"; Dataset S1) using standard methods of HF/HNO_3 leaching, froth flotation, and ion chromatography (von Blanckenburg et al., 1996). The ^{10}Be/^{9}Be ratios were measured using accelerator mass spectrometry (AMS) at the University of Cologne (relative to AMS standards KN01-6-2 and KN01-5-3) (Dewald et al., 2013) and at the PRIME Lab, Purdue University (relative to the ICN standard), consistent with the ^{10}Be half-life of 1.387 (±0.012) Myr (Chmeleff et al., 2010; Korschinek et al., 2010) and 07KNSTD standardization. The ^{26}Al splits were prepared from the oxalic acid fraction eluted from the Be columns, followed by an Al column to separate Ti from Al. ^{26}Al/^{27}Al ratios were measured using AMS at the University of Cologne relative to ^{26}Al standards KN01-5-3 and KN01-4-3, which have nominal ^{26}Al/^{27}Al ratios of 4.99×10^{-13} and 1.065×10^{-11}, respectively (Nishiizumi, 2004). The total stable ^{27}Al in the

sample was measured on a dissolved aliquot by inductively coupled plasma optical emission spectroscopy (ICP-OES) at GFZ Potsdam (e.g., Wittmann et al., 2020). For the laboratory process blank, we added 0.51 g of 1,000 ppm Merck ^{27}Al carrier that yielded a ^{26}Al/^{27}Al ratio of $(1.82 \pm 1.29) \times 10^{-15}$. One laboratory process blank ^{10}Be/^{9}Be ratio of $(1.97 \pm 0.55) \times 10^{-15}$ was subtracted from the ^{10}Be/^{9}Be ratios of samples processed at the HELGES Lab, whereas we subtracted an average ^{10}Be/^{9}Be (4.35 ± 0.46 [1σ] $\times 10^{-15}$) derived from three blanks processed alongside the samples at the PRIME Lab (Table S1 in Supporting Information S1). We propagated the uncertainties of (a) isotope ratio measurement, (b) mass of the quartz sample itself, (c) number of atoms of ^{10}Be and ^{26}Al in the laboratory process blank, and (d) mass of ^{9}Be added as a carrier and mass of stable ^{27}Al in the sample determined by ICP-OES to derive the reported uncertainties in the ^{10}Be and ^{26}Al concentrations in our samples.

3.3. Modeling CRN Concentrations

Our modeling is based on a 30-m resolution ALOS World 3D (Tadono et al., 2016) digital elevation model (DEM) of the Mohand Range, and it simulates the total accumulation of CRN at each model cell as the sum of N_E, N_B, and N_X. The governing equations for our simulation are detailed below.

3.3.1. Hinterland Paleoerosion, N_E

Mandal et al. (2021) documented ^{10}Be concentration, produced during hinterland erosion between ~6 and 0.7 Ma, by analyzing Siwalik sediment samples collected at sites where the production of CRN during recent erosion is minimal. These ^{10}Be data demonstrate that paleoerosion rates in the sediment source areas varied quasi-cyclically and increased gradually toward the present. In our modeling, we first tested a simple scenario of gradually increasing erosion rates (decreasing ^{10}Be concentrations) toward the present, assuming that the cyclic oscillations will be difficult to recover with our approach. We attributed ^{10}Be concentrations, which were acquired during paleoerosion in the sediment source region, to each site in the Mohand Range that is underlain by Siwalik rocks of depositional age t_d using the following equation:

$$N_E(x, y) = N_{10}(a + bt_d(x, y)) \tag{2}$$

where N_{10} is the ^{10}Be concentration at 10 Ma, predicted using a linear fit of the paleo ^{10}Be concentration reconstructed by Mandal et al. (2021), t_d is the time since deposition of sediment (x and y denote the spatial position of each local site underlain by the Siwalik sediment of age t_d), and a and b are parameters set such that long-term concentrations follow a gradually decreasing trend toward the present, as has been previously reported (Figure S1 in Supporting Information S1) (Mandal et al., 2021). We also tested the sensitivity of our modeling results considering an additional sinusoidal variation (see details in Supporting Information S1) in the erosion rates (temporally variable ^{10}Be concentrations; Figure S1 in Supporting Information S1).

3.3.2. Sediment Burial, N_B

^{10}Be continues to be produced in sediment after deposition in the foreland basin, with production waning as the sediment is buried. For sediments subjected to an accumulation rate of A_c (cm yr^{-1}), the concentration of ^{10}Be contributed from the burial component (N_B) at each site in the Mohand Range can be described by (Braucher et al., 2000; Charreau et al., 2011; Mandal et al., 2021):

$$N_B(x, y) = \sum_{i=1}^{3} \frac{P_i^{fb}}{\lambda - A_c(x, y)\mu_i} \left(e^{-(A_c(x,y)\mu_i - \lambda)t_d} - 1 \right) \tag{3}$$

where P_i^{fb} are the ^{10}Be production rates (at g_{qtz}^{-1} yr^{-1}; the subscript "i" denotes neutron spallation, fast muon, and stopped muon reactions) at the depositional site in the foreland basin and $\mu_i = (\rho_s/\Lambda_i)$, with ρ_s the density (g cm^{-3}) of the overlying sediment and Λ_i the attenuation lengths (g cm^{-2}).

3.3.3. Erosion of Uplifting Siwalik Rocks, N_X

Like the Siwalik Hills in the Nepal Himalaya (e.g., Hurtrez et al., 1999), we follow previous work (Allen et al., 2013; Kirby & Whipple, 2012) and assume that the Mohand Range is in a topographic steady-state, with rock uplift balanced by erosion. Under this assumption, the concentration of ^{10}Be (N_X; at g_{qtz}^{-1}) acquired during recent erosion locally for a particular site in the Mohand Range is derived using the classical equation (Lal, 1991):

$$N_X(x, y) = \sum_{i=1}^{3} \frac{P_i^{m}(x, y)}{\lambda + u(x, y)\mu_i} \tag{4}$$

where P_i^m are the ^{10}Be production rates in the Mohand Range and u is the tectonic rock uplift rate (cm yr^{-1}).

3.4. Depositional Age Model

To constrain N_E and N_B, we needed an estimate of the sediment depositional age (t_d) across the entire western Mohand Range. We used magnetostratigraphy of the Mohand and Haripur stratigraphic sections (see location in Figure 3b) (Sangode et al., 1996, 1999) as a chronological framework to assign a distinct t_d value to every cell in the DEM of the western Mohand Range. The ∼1,800-m-thick sandstone-dominated lower part of the Mohand transect has been dated between ∼9.7 and 4.8 Ma. The sandstone- and mudstone-dominated Haripur transect lies ∼50 km west of the Mohand section and covers an age range of ∼6 to <0.7 Ma. Following previous work, we assumed that the Upper Siwalik stratigraphy of the Mohand and Haripur sections have similar ages because of their proximity and association with the same structure and depositional basin (Kumar et al., 2003; Mandal et al., 2018).

We generated a depositional age map by extrapolating the magnetostratigraphy data laterally along the Mohand Range based on published geological maps (Kumar et al., 2003; Wesnousky et al., 1999), existing geological field observations (Allen et al., 2013), and pronounced lithological contrasts in the topography (Figure S2 in Supporting Information S1). The continuity of bedding along the northern and southern limbs of the Mohand fold (Figure 4a) supports this exercise. Because the estimated average sediment accumulation rates in both paleomagnetic sections are approximately uniform at ∼0.04 cm yr^{-1} (Sangode et al., 1999), we linearly interpolated ages between several tie points: (a) stratigraphic boundaries between the Middle and Upper Siwalik formations and between the Upper Siwalik Formation and Dun Gravel and (b) the axis of the Mohand fold because it marks the oldest stratigraphic age in the fold core. Based on the observed lateral continuity of the stratigraphic thicknesses of the Upper Siwalik Formation (Figure S2 in Supporting Information S1), we assumed a similar continuity for the Middle Siwalik Formation. We used the across-range horizontal gradient in stratigraphic ages to extrapolate from the Middle and Upper Siwalik boundary toward the fold axis. This part of our age model has the greatest uncertainty. However, as this part of the Mohand Range consists of old (>6 Ma) sedimentary rocks, most of the inherited CRNs are lost by radioactive decay (see Section 4.3); thus, it has the least impact on our results.

3.5. Constraints on Sediment Deposition and Burial for Determining N_B

The sediment accumulation rate (A_c) must be known to estimate the N_B (Equation 3). Magnetostratigraphy-derived local A_c is subject to the "Sadler effect" (Sadler, 1981) due to intermittent sediment deposition in the channel-floodplain system (see discussion in Mandal et al., 2021). However, at the basin scale, sediment deposition can be considered a continuous process (Sadler & Jerolmack, 2014). As the spatio-temporal channel migration patterns and sediment deposition are unconstrained, we estimated the N_B using the long-term A_c derived from magnetostratigraphic data of the Mohand and Haripur sections. These magnetostratigraphic studies constrained the accumulation rates at the time of deposition between 0.018 and 0.070 cm yr^{-1} (Sangode et al., 1996, 1999). We assigned a distinct A_c to each cell in the DEM, based on the age model of deposition (Section 3.4) and the corresponding estimated accumulation rate for each magnetozone. We assumed the wet bulk density of the overlying sediment (ρ_s) to be 2.2 g cm^{-3} (after Charreau et al. (2011) and Mandal et al. (2021)). Finally, we assumed the depocenter to be similar to the elevation of the modern Gangetic Plain (∼350 m above sea level) to scale the ^{10}Be production rate during sediment burial. Stable isotope compositions of pedogenic carbonates from the Siwalik successions support sediment deposition at low elevations (<400 m) (Sanyal et al., 2004).

3.6. Constraints on Tectonic Rock Uplift Rate for Determining N_X

The Mohand Range is an example of steady-state topography (Allen et al., 2013; Kirby & Whipple, 2012). It possesses widespread bedrock channels with well-graded elevation profiles that incise relatively uniform rock types, although some variations in channel steepness between the Middle and Upper Siwalik units have been observed. The combination of friable lithologies and efficient river incision due to high monsoon discharge likely facilitated the attainment of a topographic steady state soon after the MFT faulting began. Overall, the topography is consistent with predicted rock uplift rates estimated from the empirical relationship between river channel steepness and rock uplift rate in the Siwalik Hills of central Nepal (Kirby & Whipple, 2012). To assess the amount of ^{10}Be accumulated during erosion in the Mohand Range (N_X), we computed the spatial distribution

of rock uplift rates by constructing a kinematic model based on the MFT geometry at depth from the balanced cross-section (Figure 3c) after Mishra and Mukhopadhyay (2002). This fault geometry is constrained by (a) the seismic reflection profiles (Powers et al., 1998), (b) an exploratory well drilled near the MFT (see location in Figure 3c), and (c) surface geologic data (Mishra & Mukhopadhyay, 2002). The upper limit of the fault ramp is defined by the surface trace of the fold axis (Figure 3c). Considering that the Mohand Range uplift is associated with a fault-bend fold (e.g., Mishra & Mukhopadhyay, 2002; Powers et al., 1998; Thakur et al., 2007), the uplift rate (u, mm yr^{-1}) can be determined from the horizontal shortening rate (V, mm yr^{-1}) and the dip of the MFT at depth (α), which changes as a function of distance from the MFT surface trace (x) according to (Lavé & Avouac, 2000):

$$u(x) = V \sin \alpha(x) \tag{5}$$

Because stratigraphic exposure and topographic expression of uplift are remarkably uniform along the strike of the range (Figure S2 in Supporting Information S1), we assumed that the MFT geometry and fault slip rates are laterally invariant across the sampled area.

3.7. Additional Constraints

The least well-constrained parameters in our calculations are the horizontal shortening rate (V) and the youngest depositional age of the outcropping Upper Siwalik units, which corresponds to the maximum onset time of MFT activity (t_0). Even so, the total shortening across the Mohand Range has been constrained to 4–9 km (Mishra & Mukhopadhyay, 2002; Powers et al., 1998; V. Srivastava et al., 2018), and thus permissible combinations of V and t_0 are limited. For example, if slip along the MFT began at 0.5 Ma (speculated to be <0.773 Ma based on magnetostratigraphy; Barnes et al. (2011)), the average shortening rate would have to be 8–18 mm yr^{-1} to account for 4–9 km of total shortening. Geodetic data modeling indicates a present-day regional shortening rate of ∼18 mm yr^{-1} across this part of the Himalaya (Stevens & Avouac, 2015). However, how much of this shortening is accommodated by the MFT is unclear. Deformed Siwalik strata in the Santaurgarh Anticline (Figures 3b and 3c) indicate that active shortening along the MBT and associated footwall structures may be occurring (Thakur et al., 2007). The late Holocene slip rate along the MFT is estimated to be ≥13.8 ± 3.6 mm yr^{-1} based on a single radiocarbon-dated fluvial terrace (Wesnousky et al., 1999). This slip rate, combined with a dip of the MFT to about 30° in the study area, results in a horizontal shortening across the MFT of ≥11.9 ± 3.1 mm yr^{-1}. We tested different combinations of V and t_0 in our modeling experiments, expecting the best-fit parameter(s) to yield a total shortening of 4–9 km across the Mohand Range.

3.8. Measured Versus Modeled ^{10}Be Concentrations

After modeling the site specific ^{10}Be concentrations using Equations 2–5 and for a given combination of t_0 and V, the catchment-averaged ^{10}Be concentration in fluvial sediment ($\bar{N}$) was estimated using (Granger & Riebe, 2014):

$$\bar{N} = \frac{\int (N\varepsilon) dA}{\int \varepsilon dA} \tag{6}$$

where N and ε are site-specific concentrations (at g_{qtz}^{-1}) and erosion rates (cm yr^{-1}), respectively, and A is the sediment-contributing area (cm^2). The parameter values used in the site-specific calculations are listed in Table 1. We used a brute force approach and iterated through values of t_0 (in increments of 0.01 Myr between 0.4 and 1 Ma) and V (in increments of 0.05 mm yr^{-1} between 5 and 15 mm yr^{-1}) to find a combination that minimizes the root-mean-square error (RMSE) between measured and simulated catchment-wide concentrations of ^{10}Be. The tested ranges of t_0 and V were guided by the balanced cross-section-derived total shortening across the Mohand Range and the onset age of MFT deformation, constrained by previous studies (see Section 2.2 and 3.7). We used a Monte Carlo approach to assess the impact of analytical uncertainties on the combination of t_0 and V that minimized the RMSE. Vectors with 10,000 random ^{10}Be concentrations were generated for each sample, drawn from a normal distribution defined by the measured concentration and its 1σ uncertainty. These vectors were subsequently used to compute 10,000 combinations of t_0 and V, which minimized the RMSE. The RMSE for each combination of t_0 and V was calculated using:

Table 1
Parameters Used in the Modeling of ^{10}Be and ^{26}Al Concentrations in Sediments Eroded From the Mohand Range

Parameter	Symbol and unit	Value	References
^{10}Be decay constant	λ_{10} (yr^{-1})	4.998 ± 10^{-7}	Chmeleff et al. (2010) and Korschinek et al. (2010)
^{26}Al decay constant	λ_{26} (yr^{-1})	9.83 ± 10^{-7}	Balco et al. (2008)
Sea-level high-latitude ^{10}Be production rate:			
Neutrons	P_i (at g^{-1} yr^{-1})	4.09	Phillips et al. (2016)
Fast muons	P_j (at g^{-1} yr^{-1})	0.024	Braucher et al. (2003, 2011)
Stopped muons	P_k (at g^{-1} yr^{-1})	0.027	Braucher et al. (2003, 2011)
Attenuation length:			
Neutrons	Λ_i (g cm^{-2})	160	Lal (1991)
Fast muons	Λ_j (g cm^{-2})	4,320	Braucher et al. (2003, 2011)
Stopped muons	Λ_k (g cm^{-2})	1,500	Braucher et al. (2003, 2011)
Density:			
Unconsolidated sediment	ρ_s (g cm^{-3})	2.5	

$$\mathrm{RMSE} = \sqrt{\frac{1}{n}\sum_{i=1}^{n}\left(N_i^{\mathrm{s}} - N_i^{\mathrm{m}}\right)^2} \tag{7}$$

where N_i^{s} and N_i^{m} are the simulated and measured concentrations of ^{10}Be, respectively, and n is the number of analyzed samples.

3.9. ^{26}Al/^{10}Be Ratio

To assess the accuracy of our model for extrapolating the magnetostratigraphic ages to determine the age of sediment deposition (Section 3.4), as well as the plausibility of our assumed sediment pathway, we analyzed the ^{26}Al/^{10}Be ratio in a set of 10 fluvial sediment samples. ^{26}Al and ^{10}Be are produced in quartz at a constant ratio of 6.75 (Balco et al., 2008). Although their production rates vary with time and depth, the ^{26}Al/^{10}Be ratio remains constant. The half-lives of ^{26}Al and ^{10}Be are 0.708 ± 0.017 Myr (Nishiizumi, 2004) and 1.387 ± 0.012 Myr (Chmeleff et al., 2010; Korschinek et al., 2010), respectively. The production rate below 10 m of sediment cover is almost negligible compared to surface production. Therefore, burial to a depth >10 m isolates sediments from additional production, leading to differential decay between ^{26}Al and ^{10}Be and, hence, a systematic decrease in the ^{26}Al/^{10}Be ratio over time. When foreland basin successions are recycled, the ^{26}Al/^{10}Be ratio of these reworked sediments is governed by inherited nuclides that remain after radioactive decay (steps 1–4 in Figure 2) and nuclides produced during subsequent erosion (step 5 in Figure 2). Therefore, the ^{26}Al/^{10}Be ratio is a function of the age of source rocks and local erosion rate. Comparing measured and simulated ^{26}Al/^{10}Be ratios thus provides an additional test of the depositional age and kinematic models. We simulated the ^{26}Al/^{10}Be ratio in uplifted older foreland deposits by modeling both ^{26}Al and ^{10}Be concentrations in sediments of depositional ages spanning the last 10 Myr using the same procedure as described for ^{10}Be in Section 3.3, assuming a surface production ratio of 6.75 (Balco et al., 2008).

3.10. Sediment Flux Estimates

The sediment flux at the exit of a drainage basin depends on the catchment area and mean erosion rate. Because of this dependency, directly comparing CRN-derived sediment flux from drainage basins of different sizes is difficult. As explained in the introduction, we aimed to compare the sediment fluxes derived from the erosion of the hinterland and foreland FTBs. To do this, we estimated the mass flux of sediment per unit width (Q_{sn}; Mt km^{-1} yr^{-1}) of the Yamuna hinterland and Mohand Range using:

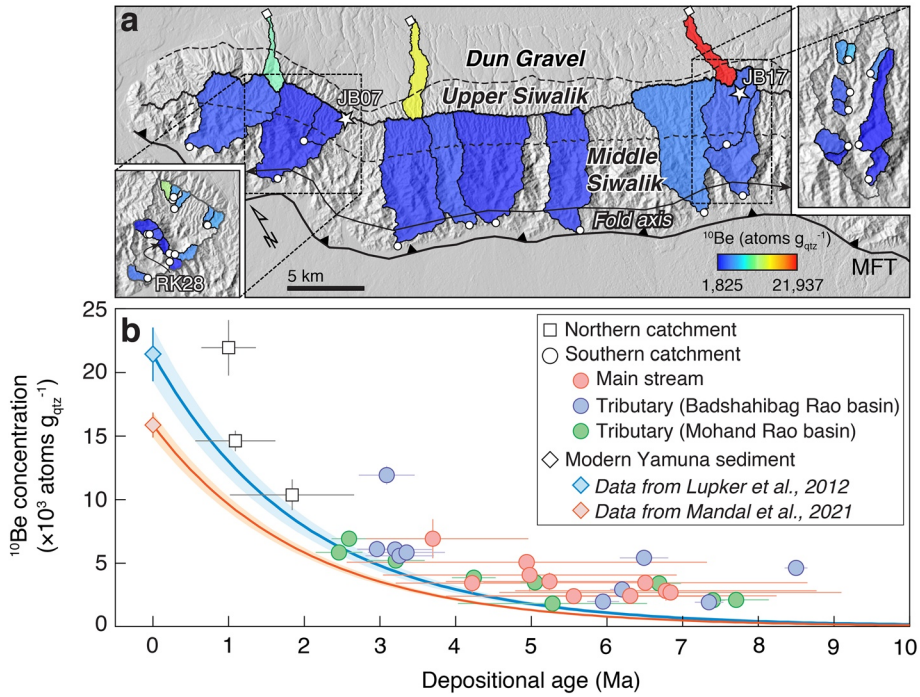

Figure 5. ^{10}Be concentrations in fluvial sediment samples from the Mohand Range. (a) Catchment-averaged ^{10}Be concentrations measured in fluvial sediment samples (polygon colors). White stars indicate locations of two bedrock samples (JB07 and JB17). (b) Measured ^{10}Be concentrations as a function of modeled depositional age. Solid colored lines and shaded envelopes (1σ uncertainty) show predicted concentrations after radioactive decay of ^{10}Be abundances in modern Yamuna hinterland sediment. The Yamuna sample analyzed by Mandal et al. (2021) integrates source areas in the Yamuna, Tons, and Giri catchments, whereas sample analyzed by Lupker et al. (2012) only integrates sources in the Yamuna and Tons catchments (see Figure 3a for sample locations). Vertical error bars correspond to the 1σ analytical uncertainty, and horizontal error bars correspond to the ±1 standard deviation from the catchment-averaged sediment age.

$$Q_{sn} = \left(\frac{\bar{\varepsilon} \rho_s A_d}{W_d} \right) \times 10^{-9} \tag{8}$$

where $\bar{\varepsilon}$ is the mean erosion rate (m yr^{-1}), ρ_s is the density of rocks undergoing erosion (kg m^{-3}), and A_d and W_d are the surface area (m^2) and along-strike width (km) of the sediment source regions, respectively. For the Yamuna hinterland, we determined W_d by calculating the arithmetic average of several basin widths measured at a regular spacing of 2 km along a direction perpendicular to the basin-length measurement. We defined basin length as the distance of a straight line that passes from the outlet to a point on the perimeter through the basin centroid (Figure S3a in Supporting Information S1). For the Mohand Range, we defined W_d as the along-strike length of the simulated domain of the Mohand Range (thick black line in Figure S3b in Supporting Information S1). We estimated sediment flux per unit width of the Yamuna hinterland $\left(Q_{sn}^{Y}\right)$ using the catchment-wide erosion rate derived from published ^{10}Be concentrations in modern fluvial sediment (Mandal et al., 2021). We estimated sediment flux per unit width of the Mohand Range $\left(Q_{sn}^{M}\right)$ using the area-weighted erosion rate predicted by modeled ^{10}Be concentrations (Section 3.3). We used the unconsolidated sediment density of 2.5 g cm^{-3}.

4. Results

4.1. Measured CRN Concentrations

The ^{10}Be concentrations in our samples range from $(1.82 \pm 0.24\ [1\sigma]) \times 10^3$ (sample RK14) to $(21.94 \pm 2.18) \times 10^3$ at g$_{qtz}^{-1}$ (sample JB16), with relative uncertainties of 6%–32% (Dataset S1; Figure 5a). Sample RK28, with a low ^{10}Be/^{9}Be ratio, exhibited a very large (~53%) relative uncertainty owing to the low current yield during

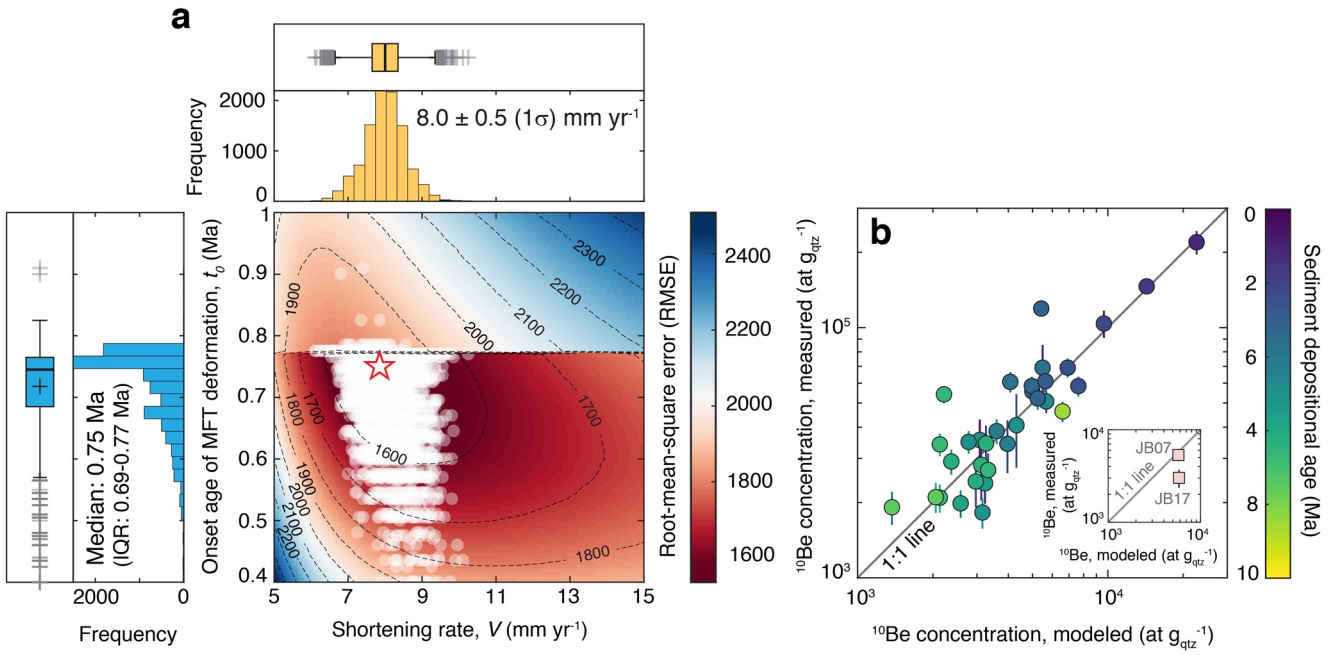

Figure 6. Modeled versus measured ^{10}Be concentrations in fluvial sediment and bedrock samples from the Mohand Range. (a) Map of root-mean-square error (RMSE) misfit between modeled (with gradually increasing paleoerosion rates toward the present) and measured ^{10}Be concentrations as a function of the shortening rate (V) and the onset age (t_0) of the Main Frontal Thrust. Light gray circles are best-fit results from the Monte Carlo simulations with 1σ analytical uncertainties. Red star is the best fit, where t_0 = 0.75 Ma and V = 7.85 mm yr^{-1}. Histograms and box-and-whisker plots at edges show the frequency distributions and statistics (thick black line = median; black cross = mean; box edges = 25th and 75th percentiles; and gray cross = outliers) of the best-fit t_0 and V from the Monte Carlo simulations, respectively. Dashed lines = RMSE contour lines. (b) Modeled versus measured catchment-averaged ^{10}Be concentrations for the best-fit parameter combination denoted by red star in panel (a). Samples are shaded according to their mean depositional age. Vertical error bars correspond to the 1σ analytical uncertainty. Inset shows the same results for the two bedrock samples using the same parameter values.

AMS measurement; hence, we excluded this sample from further analysis. The northern catchment samples have the highest ^{10}Be concentrations of (10.38 ± 1.20) × 10^3 to (21.94 ± 2.18) × 10^3 at g_{qtz}^{-1}. The southern catchment samples exhibit two main observations based on the spatial pattern of ^{10}Be concentrations (Figure 5a). First, concentrations increase toward the north (i.e., the younging direction of the north-dipping Siwalik strata; Figure S4 in Supporting Information S1). Second, along-strike variations are small, supporting our inferred similarities in stratigraphic age and tectonic structure. Overall, the data show a decline in ^{10}Be concentration as the sediments increase in age based on our depositional age model (Section 3.4), which is consistent with the loss of ^{10}Be over time due to radioactive decay (Figure 5b). The concentrations of ^{26}Al in 10 samples range from (1.12 ± 0.15) × 10^4 to (13.24 ± 2.78) × 10^4 at g_{qtz}^{-1}, yielding associated ^{26}Al/^{10}Be ratios ranging from 2.84 ± 0.48 to 7.78 ± 1.10 (Dataset S1).

4.2. Modeled Versus Measured CRN Concentrations

We tested the sensitivity of our predicted ^{10}Be concentrations in Mohand sediments with respect to two paleo-hinterland erosion (N_E) scenarios (Section 3.3.1). The RMSE misfit values in gradually decreasing N_E scenario yield minima that span a range of t_0 (*Median* = 0.75 Ma, *IQR* = 0.69–0.77 Ma) and V (*Mean* = 8.0 mm yr^{-1}, *SD* = 0.5 mm yr^{-1}) values, given the analytical uncertainties (Figure 6a). Modeled and measured ^{10}Be concentrations are well correlated (r = 0.92, p < 0.0001; Figure 6b) with the best-fit combination (t_0 = 0.75 Ma and V = 7.85 mm yr^{-1}) shown by the red star in Figure 6a. For this case, Figure 7 shows how the relative contributions (from paleoerosion, burial, and Siwalik erosion) combine to yield the present-day surface CRN concentrations across the Mohand Range. For the sinusoidally varying N_E scenario, the RMSE misfit values are also minimized over a range of t_0 (*Median* = 0.72 Ma, *IQR* = 0.64–0.76 Ma) and V (*Mean* = 9.4 mm yr^{-1}, *SD* = 0.7 mm yr^{-1}) values when accounting for analytical uncertainties (Figure S5 in Supporting Information S1). These inferred combinations of t_0 and V correspond to a total crustal shortening of 5.2–7.6 km across the Mohand Range. As the results from both N_E scenarios—within uncertainties—are similar, we refer to the results using the first,

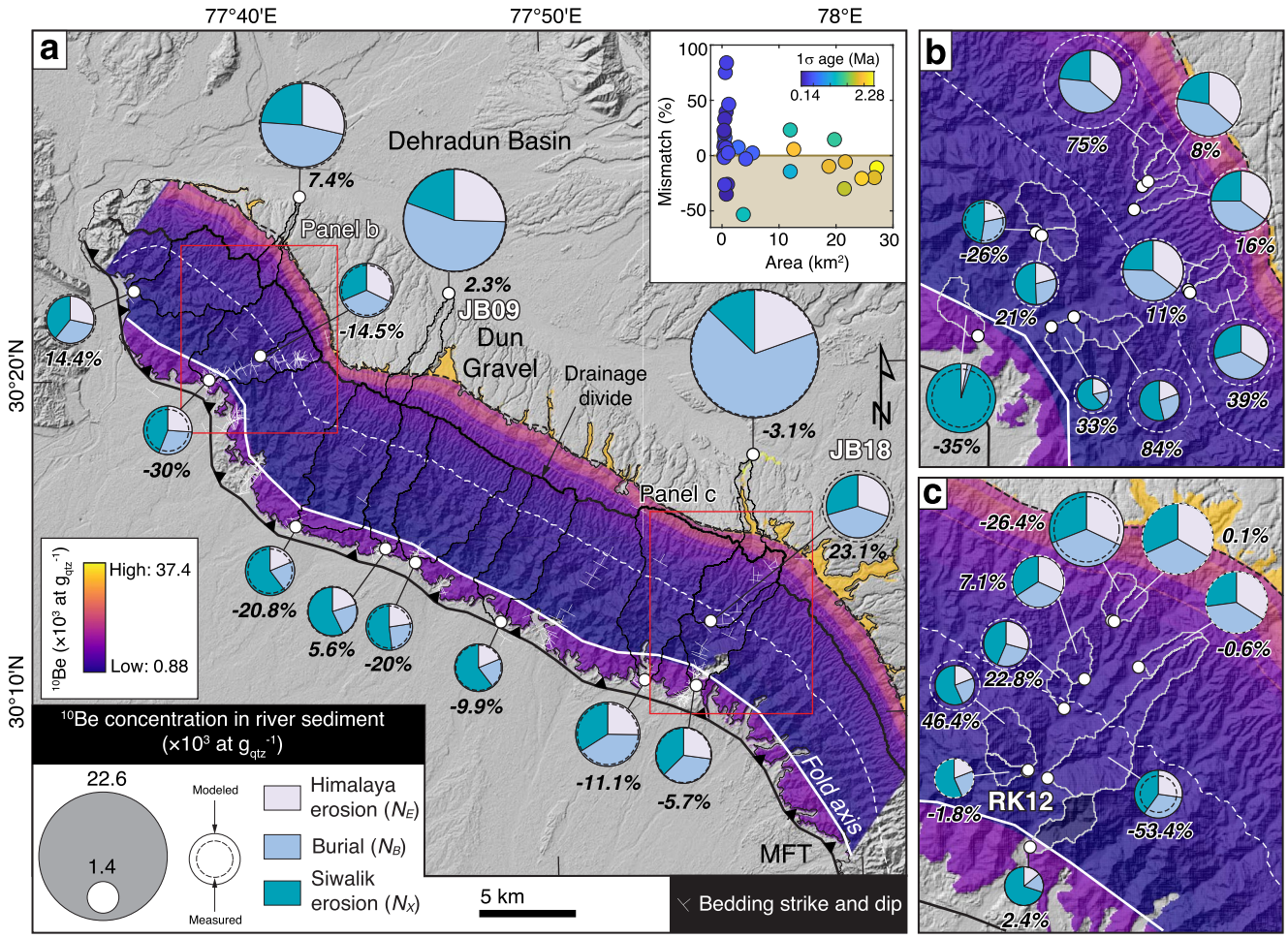

Figure 7. Modeled ^{10}Be concentrations across the western Mohand Range. (a) Map of the predicted ^{10}Be concentration in the eroded Siwalik succession, based on the best-fit scenario, as indicated by the red star in Figure 6a. (b, c) Enlarged view of sub-catchments in the Mohand Rao and Badshahibagh Rao basins. Pie charts are the relative contributions of ^{10}Be accumulated during hinterland paleoerosion, burial in the foreland basin, and subsequent erosion of the uplifting Siwalik succession to the present-day ^{10}Be concentrations in fluvial sediment samples. Percent values are the differences between the modeled and measured concentrations, where negative values mean that the model overpredicts the measured value, and positive values are the reverse. Inset in panel (a) shows the scatter plot of catchment area (km^2) versus mismatch between the modeled and measured cosmogenic radionuclide concentrations, colored by 1 standard deviation (a proxy of age range) of the mean sediment age. Bold white labels in panels (a, c) show samples highlighted in Figure 10.

simpler N_E scenario in the following discussion. Furthermore, the modeled CRN concentrations, erosion rates, and sediment fluxes reported in Table 2 and referred to in the following sections are those derived from the best-fit parameter combination.

Our simulation shows the spatial distribution of present-day ^{10}Be concentrations across the western Mohand Range, varying from 0.88×10^3 to 37.4×10^3 at g_{qtz}^{-1} (Figure 7). Generally, the concentration is lowest in old Siwalik rocks exposed near the frontal part of the Mohand Range, where the tectonic rock uplift rate is fast above the steeper MFT ramp segment. The concentration increases gradually toward the north (i.e., the younging direction of exposed Siwalik succession) until the main drainage divide. Beyond this, the progression of surface ^{10}Be concentration is erratic due to the variability in the burial component (i.e., N_B) owing to the variability in sediment accumulation rates. Using this surface ^{10}Be distribution, we estimated that the mass-averaged ^{10}Be concentration in fluvial sediments—exported from the northern flank into the Dehradun Basin—is $\sim 12.8 \times 10^3$ at g_{qtz}^{-1}, of which the majority (~86%) is inheritance (N_{inh}). In contrast, fluvial sediments shed off the southern flank into the Yamuna foredeep (in the footwall of the MFT) contain a mass-averaged ^{10}Be concentration of $\sim 2.4 \times 10^3$ at g_{qtz}^{-1}, of which ~39% is inheritance (Table 2).

At the individual catchment scale, the differences between our measured and modeled ^{10}Be concentrations are small for samples from large (>3 km^2) catchments draining foreland deposits of a broader age range. However, a

Table 2
Properties of the Hinterland and Mohand Source Areas for the Yamuna Sediment Flux Calculated in This Study (See Text)

Basin properties	Hinterland	Mohand range		Symbols and units
		Northern flank	Southern flank	
Surface area	10,213	69	204	A_d (km^2)
Width	98 ± 20 (1σ)	52[a]		W_d (km)
^{10}Be	~(13.7 ± 0.8)[b]	~12.8[c]	~2.4[c]	N (×10^3 at g$_{qtz}^{-1}$)
Erosion rate	0.98 ± 0.15[d]	1.9[e]	3.3[e]	ε (mm yr^{-1})
Sediment yield	~(2.4 ± 0.4)	~4.7	~8.2	(×10^3 t km^{-2} yr^{-1})
Sediment flux[f]	~25 ± 4	~0.3	~1.7	Q_s (Mt yr^{-1})
Sediment flux per unit width[f]	~0.27 ± 0.07	~0.07		Q_{sn} (Mt km^{-1} yr^{-1})

[a]Along-strike width of the model domain of Mohand Range. [b]Predicted concentration in hinterland sediment downstream of the confluence of the Yamuna and Giri rivers (see Supporting Information S1). [c]Modeled mass-averaged ^{10}Be concentration in fluvial sediments exported from the Mohand Range. [d]Erosion rate derived from predicted[b] ^{10}Be concentration in fluvial sediment. [e]Area-weighted mean erosion rate based on the mean ± 1σ best-fit shortening rates (V, Figure 6). [f]Cosmogenic ^{10}Be-derived sediment flux deduced from cosmogenic erosion rate.

larger mismatch (maximum 84%) exists for samples from small (<3 km^2) tributary catchments draining a narrow depositional age range (Figure 7 and Figure S4 in Supporting Information S1). These differences do not appear to show any systematic pattern with respect to their position across the Mohand Range (Figure 7) or stratigraphic age (Figure S4 in Supporting Information S1). Among the two bedrock samples, the modeled ^{10}Be concentration of sample JB07 matches quite well with the measured value, whereas the measured value of sample JB17 is ~48% less than the modeled value (Figure 6b). In contrast to fluvial sediment samples, we note that a close correspondence between the measured and modeled concentrations of bedrock samples is unexpected for episodically eroding outcrops (Small et al., 1997), which may explain the large mismatch of sample JB17.

The measured ^{26}Al concentrations also match quite well (r = 0.95, p < 0.0001) with our modeled concentrations (Figure 8a). However, like for ^{10}Be, the modeled and measured concentrations show greater differences for smaller catchments. Figure 8b and Figure S6 in Supporting Information S1 show the predicted behavior of

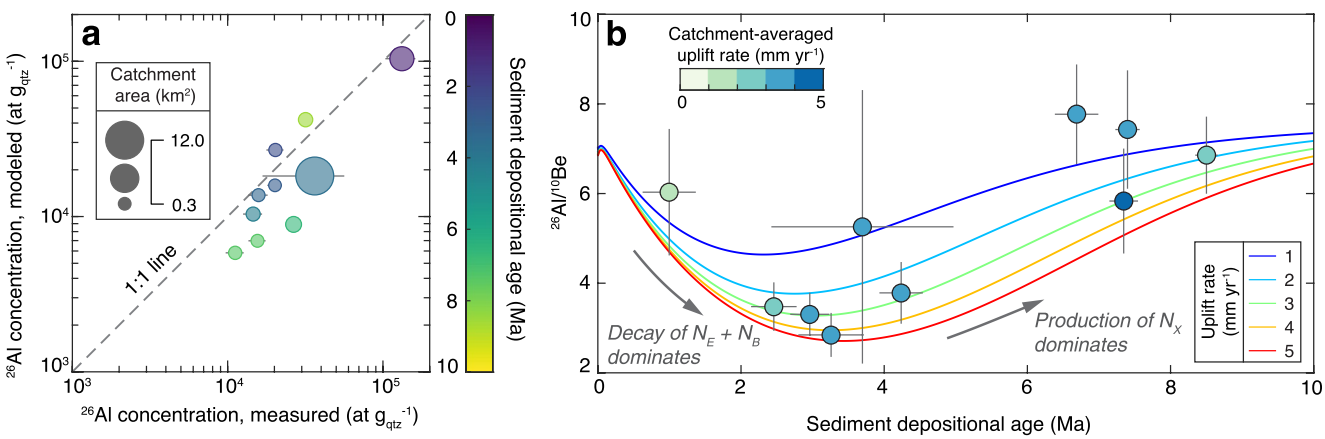

Figure 8. Modeled versus measured ^{26}Al concentrations and ^{26}Al/^{10}Be ratios in fluvial sediment samples from the Mohand Range. (a) Modeled versus measured catchment-averaged ^{26}Al concentrations for the best-fit t_0 and V (red star in Figure 6a). Samples are shaded according to their mean depositional age, and the catchment area specifies the symbol size. Horizontal error bars represent 1σ analytical uncertainty. (b) Theoretically calculated build-up of the ratios of ^{26}Al and ^{10}Be in tectonically uplifted Siwalik sediments plotted as a function of sediment age. The theoretical ratios are calculated assuming these nuclides' surface-production-rate ratio of 6.75 in quartz and that their present-day abundances result from production and decay during steps 1 to 5 in Figure 2 (see Section 3.1). Nuclides inherited from Himalayan paleoerosion and foreland burial dominate the net abundance in sediments of ages <3 Ma. The differential decay between ^{26}Al and ^{10}Be at this period set the present-day ratio. As sediments become older than ~3 Ma, the already decayed inherited components contribute less to their overall abundance; hence, the current nuclide production during Siwalik exhumation sets the present-day ratio. The colored lines depict model trajectories for uplifting Siwalik succession with uplift rates between 1 and 5 mm yr^{-1}. Colored circles represent our measured ^{26}Al/^{10}Be ratios in catchment sediments as a function of catchment-averaged sediment age. Vertical error bars correspond to the 1σ analytical uncertainty, and horizontal error bars correspond to the ±1 standard deviation from the catchment-averaged sediment age.

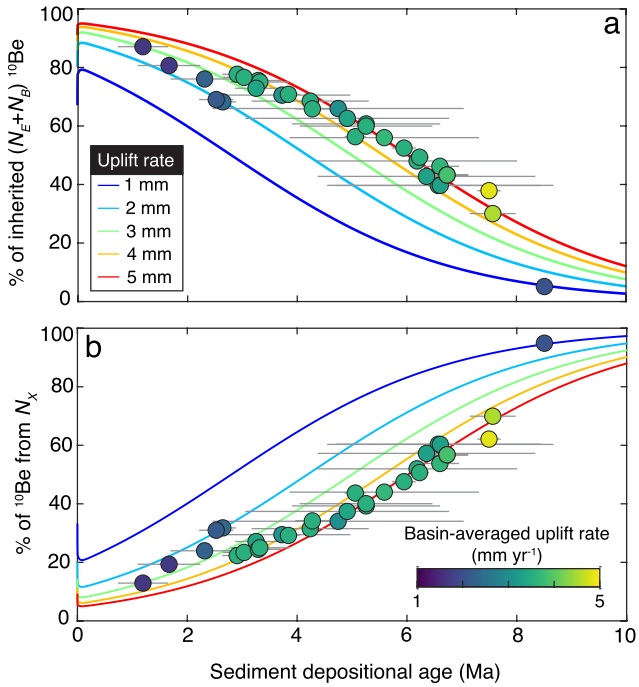

Figure 9. Relationship between sediment depositional age and abundance of ^{10}Be from (a) paleoerosion in the Himalaya (N_E) and burial in the foreland basin (N_B) and (b) subsequent erosion of the tectonically uplifted Siwalik succession (N_X). Solid lines indicate the abundance of inheritance ($N_{inh} = N_E + N_B$) and N_X as a function of sediment age and simulated for uplift rates of 1–5 mm yr^{-1}. Circles indicate the mean abundances of N_{inh} and N_X in fluvial sediment samples analyzed in this study. Circle's color indicates the catchment-wide tectonic uplift rate. The horizontal error bars represent 1 standard deviation of ages within each catchment.

the ^{26}Al/^{10}Be ratio (solid lines) in Mohand sediments spanning depositional ages of 0–10 Ma and determined using the modeled ^{10}Be and ^{26}Al concentrations for average rock uplift rates of 1–5 mm yr^{-1}. Assuming the Mohand sediment underwent a single erosion-burial-re-exhumation cycle through the foreland sediment routing system, the modeled ratio evolves toward lower values for the first few million years of sediment age when the inheritance dominates the overall abundance of CRNs (see Section 3.1). Here mainly, the differential decay between ^{26}Al and ^{10}Be sets the present-day ratio. The ratio returns toward the surface-production rate ratio as sediments become older than ~3 Ma when already decayed inherited components contribute less to the overall CRN abundance, and mainly the nuclide production during the exhumation of Siwalik strata sets the present-day ratio. Within the limits of analytical uncertainty, our measured ^{26}Al/^{10}Be ratios of 10 fluvial sediment samples, with mean depositional ages ranging from 1.00 ± 0.36 to 8.50 ± 0.15 Ma, agree with the results obtained from the model (Figure 8b). This agreement confirms that the sediment pathway is consistent with our assumption of a single erosion-burial-re-exhumation cycle.

4.3. ^{10}Be Source Partitioning

Our modeling approach enabled us to estimate the ^{10}Be contribution at each step of the sediment pathway, from hinterland paleoerosion to Siwalik erosion (Figure 2). As sediment age increases, the inheritance (N_{inh}) diminishes, while the abundance of CRNs acquired during recent erosion increases (Figure 9). Catchment-averaged inheritance in our analyzed sediment samples varies from 5% to 85% (Figures 7 and 9).

We highlight 3 representative samples (RK12, JB18, and JB09; Figure 7) to demonstrate the relative contributions of hinterland paleoerosion (N_E), burial (N_B), and recent erosion (N_X) to the ^{10}Be budget of Mohand sediment. Each sample is from a catchment that drains Siwalik rocks of different age ranges (Figure 10 and Figure S4 in Supporting Information S1). RK12 is sediment eroded from Siwalik rocks with depositional ages ≥6 Ma, JB18 from ages between ~7 and 1 Ma, and sample JB09 from a northern catchment, which comprises Siwalik rocks with ages ≤3 Ma. Our model results demonstrate contrasting contributions of N_X to the total ^{10}Be concentration in fluvial sediments recycled mostly from old (RK12) versus young (JB09) rocks (Figure 10). N_X comprises 57% of the total ^{10}Be concentration in RK12, whereas the contribution of N_X in JB09 is 19%. The contribution of N_X to the total ^{10}Be abundance in JB18, which covers a broad age range, lies between these values (28% N_X). As expected, our simulation affirms that the relative abundances of inherited (N_{inh}) and recent (N_X) CRNs in Siwalik sediments vary

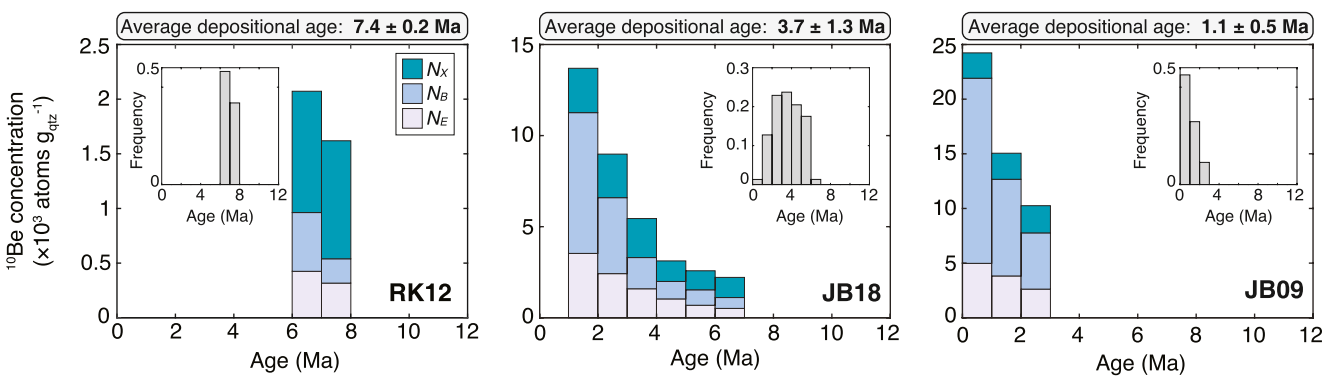

Figure 10. Modeled ^{10}Be concentrations in fluvial sediments from three representative catchments in the Mohand Range. Distribution of depositional ages within the catchment binned by 1-Myr age classes with the various contributions from three steps of cosmogenic radionuclide accumulation (N_E = paleoerosion; N_B = burial; and N_X = Siwalik erosion) compared to the total ^{10}Be concentration. Insets show relative abundances of Siwalik sediments of different ages in the catchments (locations in Figure 7). Note the differences in vertical-axis scale and that sediments >6 Ma, even if abundant, contribute little to the ^{10}Be concentration in fluvial sediment.

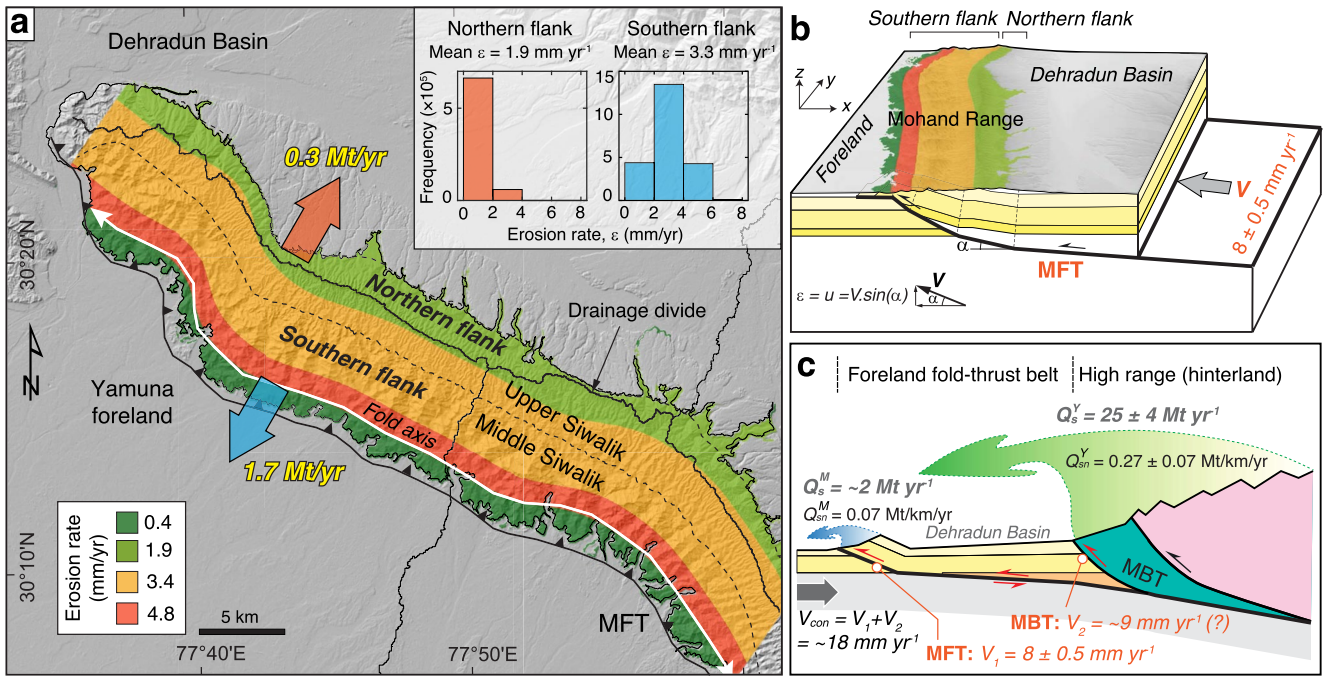

Figure 11. Erosion rates and estimated sediment flux from the Mohand Range. (a) Predicted erosion rates across the Mohand Range resulting from the best-fit shortening rate (red star in Figure 6a) of 7.85 mm yr^{-1} as constrained by our model. Yellow numbers indicate the sediment flux from the northern and southern flanks within the Yamuna Basin (i.e., west of the drainage divide). Inset histograms show the frequency distributions of the erosion rates in the Yamuna-draining northern and southern flanks of the Mohand Range. (b) Tectono-stratigraphic configuration of the Mohand fold and erosion rate along and across the range. Note that the dip (α) of the Main Frontal Thrust (MFT) is responsible for spatial variations in uplift (u) and erosion (ε) rates. Erosion rate color-coding is the same as in panel (a). (c) Schematic cross-section of the combined hinterland-foreland fold-thrust belt of the Himalaya in the study area and our estimated sediment fluxes per unit width. V_{con} represents the GPS-derived total shortening rate across the range after Stevens and Avouac (2015). V_1 indicates the recent shortening rate across the MFT deduced from our model and V_2 represents our inferred shortening rate across the Main Boundary Thrust and related structures nearby (see Section 5.2).

with their depositional ages. The low contribution of inherited CRNs in older Siwalik sediments results from loss due to radioactive decay. In contrast, much of the inherited CRNs in younger strata have not decayed, resulting in high N_E and N_B values (Figure 9). Across the Mohand Range, rocks exposed toward the north have younger depositional ages and higher inherited CRNs than those exposed toward the south. The younger Siwalik units are slowly uplifting and, consequently, have greater N_X than older Siwalik units. However, because of the low production rates in the low-relief Mohand Range, the increased N_X is insufficient to overwhelm the inherited CRNs.

4.4. Erosion Rates and Sediment Discharge

The mean ($\pm 1\sigma$) shortening rate deduced from the best-fit model results (Figure 6a) implies a spatial pattern of erosion rates spanning the western Mohand Range that vary from 0.42 ± 0.03 to 4.92 ± 0.34 mm yr^{-1} (Figure 11a). There is a ~1.2-km wide zone of high erosion rates in the northern fold limb adjacent to the hinge zone, whereas the erosion rates are the lowest in the southern limb. This abrupt decrease in erosion rate is due to the estimation of rock uplift rates based solely on the dip of the MFT (Equation 5, Figure 11b). In reality, the transition from high to low erosion rates would be more gradual as the topography is advected from a high to low rock uplift rate region (Miller & Slingerland, 2006). Likewise, northern limb erosion rates decrease step-like toward the Dehradun Basin due to the assumed kinks in the MFT plane at depth (Figure 11b). The erosion rate of the Siwalik rocks, when multiplied by their average density of 2.5 g cm^{-3}, resulted in sediment yields ranging from ~1,050 ± 70 to ~12,300 ± 800 t km^{-2} yr^{-1}. These estimates contrast the ^{10}Be-derived average sediment yield of ~2,440 ± 375 t km^{-2} yr^{-1} in the Yamuna hinterland (Table 2).

The area-weighted mean erosion rate in the northern flank of the Mohand Range is estimated to be 1.9 mm yr^{-1}. The ~69 km^2 area of outcropping Upper Siwalik rocks on the northern flank of the Mohand Range—connected with the Yamuna River—is estimated to recycle ~0.3 Mt of sediment to the Dehradun Basin annually (Table 2, Figure 11a). In contrast, the area-weighted mean erosion rate in the southern flank is 3.3 mm yr^{-1}. The ~204 km^2 area of

outcropping Upper to Middle Siwalik rocks on the southern flank—linked to the Yamuna River—is estimated to recycle ~1.7 Mt of sediment to the Yamuna foreland annually (Table 2, Figure 11a). Summing the numbers, we estimate that the total sediment flux from the Mohand Range to the Yamuna foreland $\left(Q_s^M\right)$ is ~2.0 Mt yr^{-1}, compared with ^{10}Be-derived sediment flux of ~25 ± 4 Mt yr^{-1} from the Yamuna hinterland (Q_s^Y; Table 2, Figure 11c). The sediment discharge per unit width of the Mohand Range $\left(Q_{sn}^M\right)$ is estimated to be ~0.07 Mt km^{-1} yr^{-1}, compared to the discharge per unit width of the hinterland $\left(Q_{sn}^Y\right)$ estimated to be ~0.27 ± 0.07 Mt km^{-1} yr^{-1} (Table 2, Figure 11c).

5. Discussion

5.1. Model Simplifications

Our approach demonstrates that using depositional age and structural evolution models, we can predict abundances of CRN that match the concentrations measured in modern fluvial sediments from the Mohand Range. Furthermore, we showed that CRN concentrations in reworked late Miocene to Pleistocene foreland deposits are consistent with sediment recycling in FTBs via a multi-step process (steps 1–5 in Figure 2). Our depositional age model is mainly controlled by magnetostratigraphy (Sangode et al., 1996, 1999), whereas our independently derived structural model of the frontal FTB is based primarily on a balanced cross-section (Mishra & Mukhopadhyay, 2002) constrained by seismic reflection profiles (Powers et al., 1998). Thus, consistencies between our results and existing local geological and geophysical data suggest that our approach is founded on a solid comprehension of Himalayan FTB tectonics and sediment routing systems. That said, our simulations are based on several assumptions and simplifications. In the following discussion, we examine various factors that might affect the results of our simulations.

Our method requires a regional-scale map of the stratigraphy and age of uplifting foreland deposits. For this purpose, we extrapolated a depositional age model laterally along the strike of the Mohand Range based on geological field observations (Allen et al., 2013; Kumar et al., 2003; V. Srivastava et al., 2018; Wesnousky et al., 1999). In doing so, we assumed along-strike uniformity in stratigraphic thickness and, by implication, in the age ranges of the Siwalik successions. However, local variations may exist that have not been considered. For instance, we assumed invariant sediment sourcing from the Yamuna catchment based on the provenance data (Section 2.3). This assumption might be valid for uplifted basin fills in the western Mohand Range. However, in the central part (i.e., the eastern end of our study area), there is a likelihood of at least some sediment being sourced from the Ganga catchment. We expect this scenario because the central Mohand Range is positioned nearly halfway between where the Yamuna and Ganga rivers flow through the Dehradun Basin (Figure 3a). The source rocks in both the Yamuna and Ganga catchments have similar geochemical and isotopic signatures, so provenance discrimination based on isotopic fingerprinting is difficult (Mandal et al., 2018). Therefore, if the provenance is different from what we assumed, the CRNs inherited from hinterland paleoerosion (step 1 in Figure 2) would have been different from what we envisioned. It is reassuring that the ^{10}Be concentrations in modern Ganga sediments (Dingle et al., 2018; Lupker et al., 2012; Vance et al., 2003) are similar to those measured in modern Yamuna sediments (Lupker et al., 2012; Mandal et al., 2021). Nevertheless, even if any spatial and temporal variability in provenance and hence N_E exists, our approach likely averages out this effect because we sampled catchments that integrate sediments deposited over time and space throughout the foreland depositional system. Furthermore, our model optimization is based on many samples covering a large area of the Mohand Range, thereby minimizing the effects of any local variability in N_E owing to the variability in sediment provenance. The similarity of our solutions for the two tested hinterland paleoerosion scenarios (gradual and sinusoidal variations) involving variable N_E further suggests that our simulated CRN concentrations in present-day Siwalik sediments are not susceptible to short-term variations in N_E.

Furthermore, our CRN modeling requires a regional-scale map of tectonic rock uplift rates across the Mohand Range. We constructed this map by extrapolating the subsurface geometry of the MFT from a balanced cross-section across the central Dehradun Basin (Figure 3c). We assumed that the geometry of this fault is laterally invariant along strike, supported by lateral homogeneity in the topographic appearance of the Mohand Range (Figure S2 in Supporting Information S1). The structural complexity on the southeastern side of the Mohand Range, where the MFT branches into a north-vergent thrust (Bhimgoda back-thrust in Figure 4a) that breaks the crest of the Mohand fold, lies outside of our study area and therefore poses no problem. We assumed that crustal shortening rates are temporally uniform, although it is likely that they changed since MFT deformation began. This is because the fault slip rate and the related shortening rate in a growing thrust wedge likely vary with time

(e.g., Hoth et al., 2007). However, the timescale ($\Lambda/\varepsilon\rho_s$) of the recent erosion phase (step 5, Figure 2) is relatively short (≤1.2 kyr) and, therefore, insensitive to variations in the shortening rate that occur over longer periods (Hoth et al., 2007). Nevertheless, temporal changes in the shortening rate can impact the estimated total amount of shortening in the MFT sheet predicted by our model (cf. Section 5.2).

In our reconstruction of the amounts of inherited CRN, we assumed that the lithified sediments underwent a single erosion-transport-burial cycle prior to the basin inversion (steps 1–4, Figure 2). Foreland accretion at the Himalayan front has made thrusted older foreland strata available for recycling since at least the early Pliocene (e.g., Mandal et al., 2018; van der Beek et al., 2006). This indicates that the Plio-Pleistocene foreland deposits may have undergone more than one episode of storage and reworking through the sediment routing systems. That would entail a more complicated history of inherited CRN. Older foreland deposits that could potentially be sources of the Plio-Pleistocene basin fill are the >12 Ma sedimentary rocks in the MBT footwall (Figure 3b). However, any inherited CRN in >12 Ma sediments would have decayed to <1% of the initial concentration and hence would not affect the CRN inheritance by any noticeable amount. In addition, our best-fit solution based on a single erosion-burial-re-exhumation cycle yields $^{26}Al/^{10}Be$ ratios close to the measured ones. This ground-truthing of the model results gives strength to our assumption being reasonable.

Finally, we made several implicit assumptions about the active geomorphic processes at work in the Mohand Range. We assumed that (a) erosion occurs primarily by incremental mass removal, (b) fluvial sediments are representative amalgams of particles derived from erosion of the entire source area upstream of the sampled point, and (c) these sediments are thoroughly mixed. However, our field observations suggest that the combination of friable sandstones and high discharge during monsoons facilitates sporadic meter-scale slope failures of small areal extent. The stochastic addition of CRN-depleted sediment caused by landslides, for example, could dilute the average source area ^{10}Be signals, resulting in an underestimation of the ^{10}Be concentration in fluvial sediment samples (Dingle et al., 2018; Niemi et al., 2005). Our sampled catchments have drainage areas between 0.3 and 27.1 km^2 (Figure 7). The violation of the assumption of a steady state between CRN production and their removal by erosion due to the landsliding is expected in catchments with smaller drainage areas (e.g., Niemi et al., 2005). However, the mismatch between our simulated and measured CRN concentrations occurs independent of drainage areas (Figure 7); hence it can not be attributed to episodic slope failures. Instead, small (<3 km^2) catchments drain Siwalik strata of a narrower depositional age range; thus, their modeled CRN concentrations are sensitive to any inaccuracies in depositional ages and concomitant sediment accumulation rates. We think this fact more likely explains the larger mismatch between our modeled and measured CRN concentrations in sediments sampled from small catchments.

In summary, our approach for determining CRN-derived erosion rates of a frontal FTB comprised of older foreland basin successions requires local constraints and several assumptions. The Mohand Range currently stands as one of the best locations in the Himalaya, where the availability of comprehensive data sets and field observations enabled us to test this approach. The remaining uncertainties in our underlying assumptions may have played a role in the mismatch between measured and simulated CRN concentrations. However, these uncertainties are unlikely to significantly impact our model results because our best-fit solution is derived from many samples, making it reasonably robust to being overly influenced by individual outliers.

5.2. Partitioning of Shortening at the Himalayan Front

Regardless of the variability in shortening rate over time, our modeling results suggest 5.2–7.6 km of total shortening across the Mohand Range, which is consistent with previous shortening estimates of 4–9 km based on balanced cross-section studies (Mishra & Mukhopadhyay, 2002; Powers et al., 1998; V. Srivastava et al., 2018). Our estimate is based on forward modeling present-day CRN concentration in uplifted Siwalik sediment as a sum of accumulation during three steps of the sediment pathway inferred from sediment depositional age and kinematic models, which are all plausible but not unique solutions. The ^{10}Be data are also insensitive to the variability in the shortening rate over time. In addition, the relative scarcity of samples covering the youngest period of deposition (Figure 5 and Figure S4 in Supporting Information S1) makes pinpointing the commencement of the MFT challenging. Slip on the MFT may have started sooner or later, and the shortening rate could have been more varied in the past.

With these uncertainties in mind, our estimated shortening rate of 7.5–10.1 mm yr^{-1} across the MFT in the Dehradun Basin is comparable to earlier documented shortening rates (11 ± 5 mm yr^{-1}; Powers et al. (1998);

11.9 ± 3.1 mm yr^{-1}; Wesnousky et al. (1999)). However, when compared to the current GPS-derived shortening rate of ∼18 mm yr^{-1} across the entire width of the Himalaya (Stevens & Avouac, 2015), our results indicate a shortening rate deficit of approximately 50%. The rate of stratigraphic onlap of the Siwalik Group onto the Himalayan foredeep is estimated to be between 15 and 20 mm yr^{-1}, which is comparable to the present-day shortening rate (Lyon-Caen & Molnar, 1985; Mugnier & Huyghe, 2006). Based on this argument, we do not envisage that the shortening rate across the Himalaya varied significantly during the development of the Mohand Range. Instead, a significant proportion of the crustal shortening across the Himalaya must have been accommodated by other active structures. A likely candidate is the MBT and its footwall imbricate structures, which are considered to have accommodated some late Pleistocene to Holocene out-of-sequence activity (Mishra & Mukhopadhyay, 2002; Thakur et al., 2007). This partitioning of crustal shortening in the Dehradun Basin is quite similar to that inferred from the Kangra Basin, located ∼200 km northwest of the study area (Figure 1). In the Kangra Basin, Dey et al. (2016) inferred that the out-of-sequence Jwalamukhi Thrust has accommodated about 40%–60% of the total Sub-Himalayan shortening over the Holocene. Even so, these observations contrast with studies in the central and eastern Himalayas, where the Holocene shortening rate along the MFT—estimated from deformed fluvial terraces—are ∼21 ± 1.5 mm yr^{-1} (Lavé & Avouac, 2000) and 23.4 ± 6.2 mm yr^{-1} (Burgess et al., 2012), which agrees well with the GPS-derived shortening rate across the Himalaya (Stevens & Avouac, 2015). The study by Burgess et al. (2012) further inferred that the total shortening across the MFT zone in the eastern Himalaya is distributed across multiple active structures over the 10 km wide décollement.

Support for the recent activity of the MBT and related structures comes from the published ^{10}Be-derived catchment-averaged erosion rates of the Lesser Himalaya, upstream of the Dehradun Basin. Approximately 10 km north of the MBT, the erosion rates in the Yamuna tributary catchments increase southward (Scherler et al., 2014) within a zone where two tributaries also feature well-defined knickpoints clustered at ∼1,130–1,230 m elevation (Figure S7 in Supporting Information S1). To the north of this zone, erosion rates vary from 0.13 ± 0.01 to 0.22 ± 0.02 mm yr^{-1}. To the south, erosion rates abruptly jump to approximately 0.55 ± 0.04 mm yr^{-1}. We note that any change in lithology does not accompany this shift in erosion rates; rocks to the north and south of this transition are both metasedimentary rocks of the outer Lesser Himalayan Sequence. Based on these observations, we speculate that the MBT and related nearby structures may have accommodated approximately 50% of the Holocene shortening across the Dehradun Basin.

Coeval active shortening on multiple basin-bounding faults could account for the coupling between tectonics and accommodation and, by implication, sedimentation in the Dehradun Basin. The interplay between subsidence-controlled accommodation space and sediment supply from the hinterland FTB dictates the longevity of the wedge-top basin (Ori & Friend, 1984). A potential mechanism that can modulate the relationship between accommodation space and sediment supply is the slip along the upstream thrust fault that the MBT and related structures nearby would have provided. The orogenic load induced by shortening on these structures may be driving local subsidence that, in turn, facilitates the sediment accommodation and hence the entrapment of Dun Gravel in the basin.

5.3. Sediment Recycling From Older Foreland Successions

Our framework provides a first-order estimate of recycled sediment flux from the Mohand Range into the proximal Himalayan foreland basin. ^{10}Be-derived sediment flux from the Yamuna hinterland $\left(Q_s^Y\right)$ exceeds the flux from the Mohand Range $\left(Q_s^M\right)$ by a factor of ∼13 (Figure 11c). However, the modern foreland basin receives recycled sediment input not only from the Mohand Range but also laterally from other structures, such as the Santaurgarh and Dhanaura folds, and through older foreland material recycling in the MBT footwall (Figure 3). Neglecting these contributions underestimates the relative contribution of recycling to the sediment load supplied by the Yamuna River to the foreland basin. Therefore, an estimate based on the normalized sediment flux per unit width of the Yamuna hinterland $\left(Q_{sn}^Y\right)$ and Mohand Range $\left(Q_{sn}^M\right)$ may alleviate the problem of undefined sources. The tectonomorphic setting of the Himalaya at this longitude lends itself to this exercise, because sediment fluxes of the hinterland and foreland FTBs are well partitioned by the Dehradun Basin (Figure 11). The results of this approach suggest that recycling in the frontal Siwalik range accounts for ∼21% ± 5% of the total sediment flux per unit width of the combined hinterland-foreland system of the Himalaya, at least at the longitude of the Dehradun Basin.

The influx of recycled material has been shown to alter the CRN concentrations of sediments eroded from the hinterland source regions during transit to the foreland (e.g., Fülöp et al., 2020; Hu et al., 2011). Rapid rock uplift

and erosion rates in the Mohand Range result in low additional CRN accumulation. While the MFT geometry at depth modulates the recent rate of erosion and attendant CRN production, the age of stratigraphic succession governs the CRN inheritance. Our results demonstrate that these factors produce a spatial variability in recycled sediment CRN concentrations across the Mohand Range that vary by nearly a factor of 40, leading to a ca. 4-fold difference in mean CRN concentrations in sediments recycling from the northern and southern flanks. Using ^{10}Be concentrations previously measured in sediments from the Yamuna-Tons and Giri rivers near their confluence in the Dehradun Basin by Mandal et al. (2021) (Figure 12a), we estimate the ^{10}Be concentration in mainstream sediment to be around $(13.7 \pm 0.8) \times 10^3$ at g_{qtz}^{-1} (see details in Supporting Information S1). This hinterland ^{10}Be concentration is comparable to our predicted average ^{10}Be concentration of 12.8×10^3 at g_{qtz}^{-1} in recycled Siwalik sediment shed off the northern flank of the Mohand Range. This observation suggests that the northern flank-derived sediment does not alter the hinterland signal perceptibly. Indeed, the previously measured (Mandal et al., 2021) ^{10}Be concentration of $(15.9 \pm 1.0) \times 10^3$ at g_{qtz}^{-1} in mainstream sediment—downstream of the confluence of the Yamuna and Asan rivers that integrate sediment shed off the northern flank—is statistically indistinguishable from the upstream sediment ^{10}Be concentration (Figure 12a). This resemblance implies that, despite being mixed with recycled material, hinterland sediments sequestered in the Dehradun Basin retain ^{10}Be concentrations equivalent to those acquired during source area erosion.

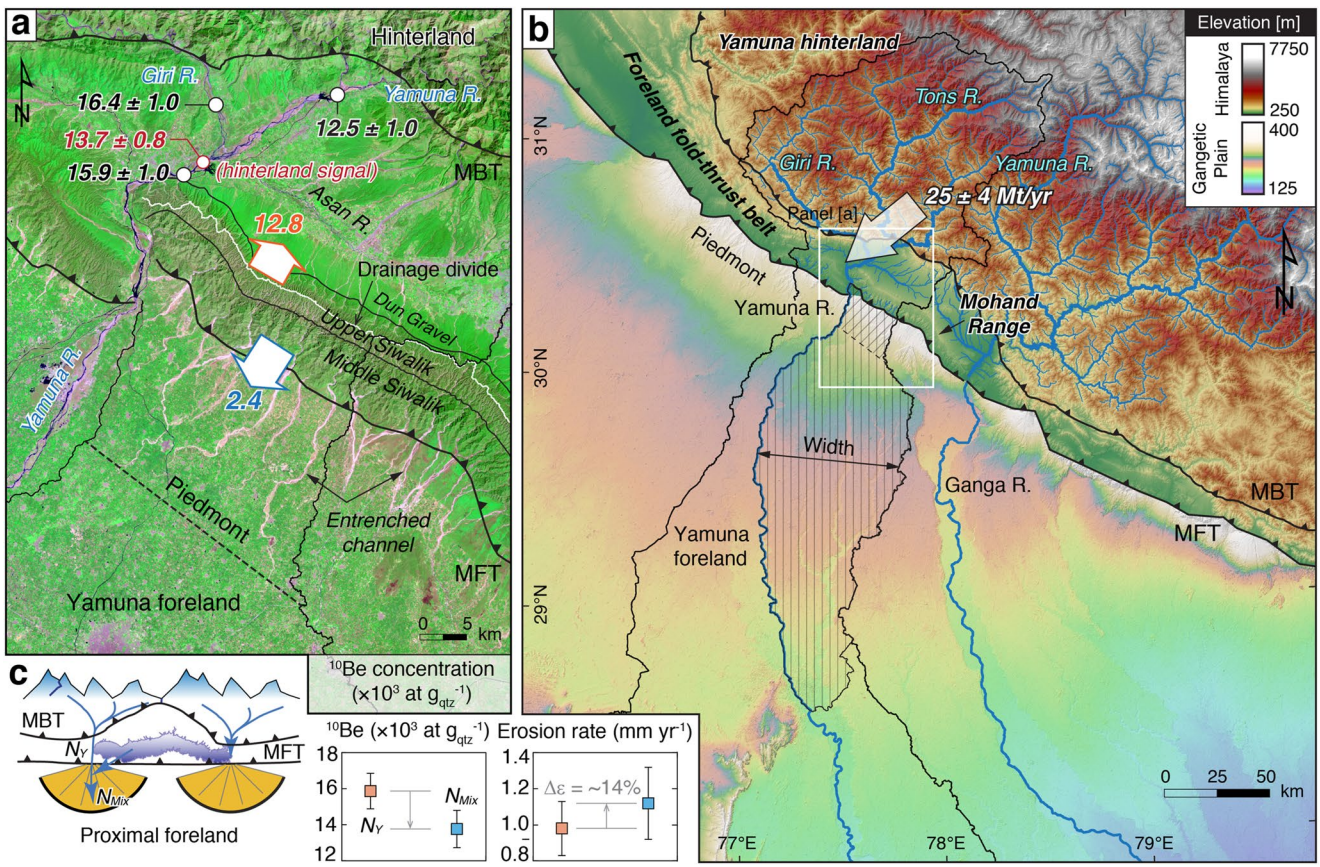

Figure 12. Overview of the proximal Himalayan foreland basin and ^{10}Be concentration in fluvial sediments along the Yamuna sediment routing system. (a) ^{10}Be concentrations in sediments from the Yamuna hinterland after Mandal et al. (2021) and our modeled mass-averaged ^{10}Be concentrations in sediments recycled from the northern and southern flanks of the Mohand Range. Note that the hinterland ^{10}Be signal refers to the concentration in fluvial sediment downstream of the confluence between the Yamuna and Giri rivers that integrate sediments eroded from the high Himalaya. Background is the Landsat 8 image of the study area. (b) Overview of the proximal Himalayan foreland basin and tributary fan system adjacent to the Mohand Range. Hatched zone represents the proximal foreland region, where piedmont rivers, originating from the Mohand Range, deposit sediment prior to their eventual confluence with the Yamuna River. (c) Predicted ^{10}Be concentrations and calculated erosion rates when low ^{10}Be sediment recycled from the southern flank of the Mohand Range is admixed to hinterland sediment with in the proximal foreland. N_Y = pristine ^{10}Be concentration in hinterland sediment (i.e., the hinterland signal in panel (a)). The concentration of mixed sediment (N_{Mix}) is predicted using a simple binary mixing approach and per unit width sediment fluxes (see Section 5.3). ^{10}Be-derived erosion rate estimates are based on the mean ^{10}Be production rate in the Yamuna catchment, upstream of the Main Boundary Thrust. $\Delta\varepsilon$ indicates the higher than actual erosion rate in the hinterland based on the N_{Mix}.

However, as the Yamuna River crosses the mountain-front and debouches into the Gangetic Plain, southern flank recycling introduces Siwalik sediment with a low ^{10}Be concentration. In contrast to the Dehradun Basin, any change in the hinterland signal while routing through the proximal Gangetic Plain is additionally controlled by the filled state of the alluvial piedmont zone (i.e., the proximal foredeep region) or, alternatively, the percentage flux of recycled mass that bypasses the piedmont and eventually enters the mainstream. The subsidence rate beneath the Yamuna piedmont is estimated to be 0.04 ± 0.03 cm yr^{-1} (Dingle et al., 2016), which is equivalent to the magnetostratigraphy-derived long-term mean sediment accumulation rate of ∼0.04 cm yr^{-1} (Sangode et al., 1999). These estimated subsidence and sedimentation rates are significantly lower than our estimated mean erosion rate of 3.3 mm yr^{-1} across the southern flank of the Mohand Range. Using the previously documented subsidence rate beneath the Yamuna piedmont (Dingle et al., 2016), our estimate suggests that to sequester the equivalent volume of recycled sediment discharge from the southern flank, a basin surface area of ca. $(2.6 \pm 2.1) \times 10^3$ km^2 is required across the Yamuna foreland. The examination of fluvial form in the proximal Yamuna foreland using Landsat imageries and DEM reveals that the region where piedmont rivers, originating from the southern flank of the Mohand Range, deposit sediment prior to their eventual confluence with the Yamuna River, covers an approximate area of 8.9×10^3 km^2 (indicated by the hatched region in Figure 12b). As a result, sediment originating from the southern flank can be effectively stored in the proximal foreland region. The average width of this piedmont depositional lobe is estimated to be ∼45 ± 16 km. Hence, a strike transverse length of ∼65 ± 61 km is required to accommodate the recycled mass throughout the piedmont depositional lobe. Channels in the alluvial piedmont are entrenched for up to ∼20 km from the mountain-front, according to our analysis of Landsat imageries and field observations. Channels downstream of this limit are unconfined, resulting in the possibility of mixing between the hinterland and recycled sediments owing to lateral channel migration across the fan. Based on the current subsidence rate, this ∼20-km wide piedmont zone (shown by the cross-hatched area in Figure 12b) has the potential to store around 0.5 ± 0.4 Mt of sediment annually, which suggests that ∼31% ± 25% of the annual recycled mass flux accumulates in the piedmont zone with pristine CRN signatures. On a geological time scale, this deposition of recycled material in the piedmont without mingling with hinterland sediment leads to the trapping of CRN fingerprints within a recycling loop. The remaining flux of recycled material is prone to mixing with hinterland sediment.

Using a simple sediment mixing model for two source regions (i.e., the hinterland and Siwalik range), each with different ^{10}Be concentrations, we can predict the ^{10}Be concentration of the sediment mixture (N_{Mix}) downstream of the piedmont as:

$$N_{\mathrm{Mix}} = f_{\mathrm{M}} \times N_{\mathrm{M}} + (1 - f_{\mathrm{M}}) \times N_{\mathrm{Y}} \tag{9}$$

where N_{Y} is the ^{10}Be concentration in Yamuna hinterland sediment, N_{M} is our predicted average ^{10}Be concentration in sediment conveyed from the southern flank of the Mohand Range into the Yamuna foreland, and f_{M} is the fraction of sediment flux (per unit width of the Mohand Range; $Q_{\mathrm{sn}}^{\mathrm{M}}$) that is bypassing the piedmont zone and thus liable to mix with the hinterland flux. If ∼69% ± 25% of the $Q_{\mathrm{sn}}^{\mathrm{M}}$ is ultimately delivered to the proximal Yamuna foreland and is eventually mixed with hinterland sediment, the ^{10}Be concentration in the resultant mixed sediment (N_{Mix}) is estimated to be ca. $(11.9 \pm 0.8) \times 10^3$ at $g_{\mathrm{qtz}}{}^{-1}$ (Figure 12c). Given that the CRN concentration is inversely proportional to the erosion rate, a simple inversion of the mixed sediment ^{10}Be concentration would overestimate the actual Yamuna hinterland erosion rate by ∼14% (Figure 12c). We note that this prediction seems to contradict the previous conclusion by Lupker et al. (2012), which suggests no systematic evolution of sediment ^{10}Be concentration during transit through the Gangetic Plain. However, most sediment samples analyzed by Lupker et al. (2012) are from the distal Gangetic Plain, where a multitude of internal processes, including sediment transport and floodplain reworking, can introduce additional CRNs, as demonstrated by Ben-Israel et al. (2022). Consequently, in the distal Gangetic Plain, these processes can obscure the signal of ^{10}Be lowering caused by the recycling of older foreland deposits. Indeed, published (Lupker et al., 2012) ^{10}Be concentrations in three sediment samples from the proximal Karnali foreland (PB80, LO743, and BR355), when compared with the concentration in mainstream sediment sample (CA10-5), upstream of the foreland FTB, reveal a ∼2–5 fold decrease in ^{10}Be concentration, consistent with our prediction.

Sediments from the Himalayan hinterland carry a ^{26}Al-^{10}Be signal of their source area. However, incorporating the recycled sediment while routing through the proximal foreland may obscure this signal. Our model prediction shows that sediments exported from the northern and southern flanks of the Mohand

Range carry ^{26}Al-^{10}Be inventories with a mass-averaged ratio of 4.2 and 3.9, respectively. Assuming that these nuclides are produced at a ratio of 6.75 (Balco et al., 2008) in hinterland sediments, the admixture of ∼69% ± 25% (see discussion above) of the sediment flux per unit width of the Mohand Range and mass flux per unit width of the Yamuna hinterland result in a ^{26}Al/^{10}Be ratio of 6.66 ± 0.96. Because analytical errors for ^{26}Al are often substantially bigger than those for ^{10}Be, determination of the alteration of this ratio in proximal foreland sediment may be challenging. The ^{26}Al/^{10}Be ratios measured in Gangetic Plain sediment by Wittmann et al. (2020), are within analytical uncertainties close to the surface production-rate ratio, confirming our prediction. However, if recycled sediment escapes mixing with hinterland sediment en route to the foreland sink, as is likely the case in the piedmont zone, without considering this effect, the interpretation of burial-storage history based on ^{26}Al-^{10}Be inventories would indicate a million-year lag in the foreland routing system.

The anticipated modification of the hinterland CRN signal by mixing with recycled foreland deposits in the proximal Himalayan foreland necessitates more research, ideally from many locations, in order to better understand environmental signal propagation across the foreland routing system. The flux of recycled mass into the foreland basin along the Himalayan arc is expected to vary depending on the catchment surface areas underlain by tectonically accreted older foreland successions and their erosion rates, which depend in part on the partitioning of shortening across the foreland FTB. Except for the Kangra Basin and the Bhutan Himalaya, where structurally cannibalized late Neogene to Pleistocene foreland successions are exposed and eroding over much larger and smaller areas, respectively, the situation analyzed in this study may also apply to other parts of the Himalayan FTB (Figure 1). Additional modifications apply where most or all of the shortening occurs on the MFT, as in central Nepal (e.g., Lavé & Avouac, 2000). In our study area, we deduce that the MFT accounts for only ∼50% of the shortening, with the remaining occurring on the MBT and nearby structures. Because such structural activity is unlikely to be sustained in the long term, all of the shortening is expected to occur on the MFT at some point in the future. In such a situation, our modeling predicts that the sediment flux from the Mohand Range would double, but the ^{10}Be concentration would decrease due to the higher erosion rates. As a result, the predicted modification of the hinterland CRN signal would increase proportionally.

6. Summary and Conclusions

This study presents a new approach for determining erosion rates across a foreland fold-thrust belt, where sedimentary successions still have large cosmogenic radionuclides inherited from past erosion in the hinterland and deposition-burial in the foreland basin. When applied to the Mohand Range, an emerging fault-related fold in the frontal part of the northwestern Himalaya, this approach predicts erosion rates across the Mohand Range that vary between ca. 0.42 ± 0.03 and ca. 4.92 ± 0.34 mm yr^{-1}. The associated sediment flux suggests ca. 2.0 Mt of sediment recycling annually from the Mohand Range, which is then transported to the adjacent Yamuna foreland. Our estimates suggest that—at least at the longitude of the Dehradun Basin—ca. 21% ± 5% of the modern sediment flux leaving a unit width of the Himalaya originates through sediment recycling in the foreland fold-thrust belt. Furthermore, our simulations, solving for the combination of the timing of initiation of slip on the MFT and attendant shortening rate to explain the measured cosmogenic radionuclides ^{10}Be and ^{26}Al concentrations in present-day fluvial sediments, indicate initiation of uplift above the MFT occurred at $0.75^{+0.02}_{-0.06}$ Ma and that the recent crustal shortening rate across the Mohand Range is 8.0 ± 0.5 mm yr^{-1}. Our simulation predicts that sediments exported from the northern and southern flanks of the Mohand Range into the wedge-top (Dehradun Basin) and proximal Yamuna foreland, respectively, carry an average ^{10}Be concentration of $\sim 12.8 \times 10^3$ at g_{qtz}^{-1} and $\sim 2.4 \times 10^3$ at g_{qtz}^{-1}. ∼86% and ∼39% of these ^{10}Be abundances in northern- and southern flank-derived sediments, respectively, are inherited from the previous erosion-deposition-burial cycle. The spatial variability of CRN concentration in recycled sediment across the frontal Himalayan range implies that the ^{10}Be signal of high Himalayan erosion likely alters while routing through the proximal Himalayan foreland basin.

Conflict of Interest

The authors declare no conflicts of interest relevant to this study.

Data Availability Statement

Cosmogenic ^{10}Be and ^{26}Al analytical data (Dataset S1), the depositional age map of uplifted older foreland sediments across the western Mohand Range (Dataset S2), the map of best-fit ^{10}Be concentration inherited from Himalayan paleoerosion (Dataset S3), the map of best-fit ^{10}Be concentration inherited from sediment burial in the foreland (Dataset S4), the map of best-fit ^{10}Be concentration produced during modern erosion in the Mohand Range (Dataset S5), and the map of best-fit uplift/erosion rates across the western Mohand Range (Dataset S6) are available from Mandal et al. (2023) in the repository at https://doi.org/10.5880/fidgeo.2023.027.

Acknowledgments
This research was supported by the German Science Foundation DFG-Grant SCHE1676/3-1 to D. Scherler, Science and Engineering Research Board, Department of Science and Technology, Government of India, Grant SRG/2019/000005 to S.K. Mandal, NSF Earth Sciences Postdoctoral Fellowship (GEO/EAR 0814723) to J.B. Barnes, and UKIERI Grant SA07-06F to A.L. Densmore. The authors thank Hella Wittmann for her help and advice in sample preparation for the ^{10}Be and ^{26}Al analysis. Stefan Heinze and Steven Binnie from the University of Cologne are thanked for performing AMS measurements. Cathrin Schulz is thanked for laboratory support. Finally, we thank Mike Oskin, Michal Ben-Israel, and an anonymous reviewer for their insightful reviews that helped improve the manuscript.

References

Allen, G. H., Barnes, J. B., Pavelsky, T. M., & Kirby, E. (2013). Lithologic and tectonic controls on bedrock channel form at the northwest Himalayan front. *Journal of Geophysical Research: Earth Surface*, *118*(3), 1806–1825. https://doi.org/10.1002/jgrf.20113

Andermann, C., Crave, A., Gloaguen, R., Davy, P., & Bonnet, S. (2012). Connecting source and transport: Suspended sediments in the Nepal Himalayas. *Earth and Planetary Science Letters*, *351–352*, 158–170. https://doi.org/10.1016/j.epsl.2012.06.059

Avouac, J.-P. (2015). Mountain building: From earthquakes to geologic deformation. In *Treatise on geophysics* (pp. 381–432). Elsevier. https://doi.org/10.1016/b978-0-444-53802-4.00120-2

Balco, G., Stone, J. O., Lifton, N. A., & Dunai, T. J. (2008). A complete and easily accessible means of calculating surface exposure ages or erosion rates from ^{10}Be and ^{26}Al measurements. *Quaternary Geochronology*, *3*(3), 174–195. https://doi.org/10.1016/j.quageo.2007.12.001

Barnes, J. B., Densmore, A. L., Mukul, M., Sinha, R., Jain, V., & Tandon, S. K. (2011). Interplay between faulting and base level in the development of Himalayan frontal fold topography. *Journal of Geophysical Research*, *116*(F3), F03012. https://doi.org/10.1029/2010jf001841

Ben-Israel, M., Armon, M., Team, A., & Matmon, A. (2022). Sediment residence times in large rivers quantified using a cosmogenic nuclides based transport model and implications for buffering of continental erosion signals. *Journal of Geophysical Research: Earth Surface*, *127*(5), e2021JF006417. https://doi.org/10.1029/2021JF006417

Bierman, P. R., & Steig, E. J. (1996). Estimating rates of denudation using cosmogenic isotope abundances in sediment. *Earth Surface Processes and Landforms*, *21*(2), 125–139. https://doi.org/10.1002/(sici)1096-9837(199602)21:2⟨125::aid-esp511⟩3.0.co;2-8

Braucher, R., Bourlès, D., Brown, E., Colin, F., Muller, J.-P., Braun, J.-J., et al. (2000). Application of in situ-produced cosmogenic ^{10}Be and ^{26}Al to the study of lateritic soil development in tropical forest: Theory and examples from Cameroon and Gabon. *Chemical Geology*, *170*(1–4), 95–111. https://doi.org/10.1016/s0009-2541(99)00243-0

Braucher, R., Brown, E., Bourlès, D., & Colin, F. (2003). In situ produced ^{10}Be measurements at great depths: Implications for production rates by fast muons. *Earth and Planetary Science Letters*, *211*(3–4), 251–258. https://doi.org/10.1016/s0012-821x(03)00205-x

Braucher, R., Merchel, S., Borgomano, J., & Bourlès, D. (2011). Production of cosmogenic radionuclides at great depth: A multi element approach. *Earth and Planetary Science Letters*, *309*(1–2), 1–9. https://doi.org/10.1016/j.epsl.2011.06.036

Brown, E. T., Stallard, R. F., Larsen, M. C., Raisbeck, G. M., & Yiou, F. (1995). Denudation rates determined from the accumulation of in situ-produced ^{10}Be in the Luquillo Experimental Forest, Puerto Rico. *Earth and Planetary Science Letters*, *129*(1–4), 193–202. https://doi.org/10.1016/0012-821x(94)00249-x

Burgess, W. P., Yin, A., Dubey, C. S., Shen, Z.-K., & Kelty, T. K. (2012). Holocene shortening across the main frontal thrust zone in the eastern Himalaya. *Earth and Planetary Science Letters*, *357–358*, 152–167. https://doi.org/10.1016/j.epsl.2012.09.040

Caldwell, W. B., Klemperer, S. L., Lawrence, J. F., Rai, S. S., & Ashish (2013). Characterizing the main Himalayan thrust in the Garhwal Himalaya, India with receiver function CCP stacking. *Earth and Planetary Science Letters*, *367*, 15–27. https://doi.org/10.1016/j.epsl.2013.02.009

Charreau, J., Blard, P.-H., Puchol, N., Avouac, J.-P., Lallier-Vergès, E., Bourlès, D., et al. (2011). Paleo-erosion rates in Central Asia since 9 Ma: A transient increase at the onset of Quaternary glaciations? *Earth and Planetary Science Letters*, *304*(1–2), 85–92. https://doi.org/10.1016/j.epsl.2011.01.018

Charreau, J., Lavé, J., France-Lanord, C., Puchol, N., Blard, P.-H., Pik, R., & Gajurel, A. P. (2020). A 6 Ma record of palaeodenudation in the central Himalayas from in situ cosmogenic ^{10}Be in the Surai section. *Basin Research*, *33*(2), 1218–1239. https://doi.org/10.1111/bre.12511

Chmeleff, J., von Blanckenburg, F., Kossert, K., & Jakob, D. (2010). Determination of the ^{10}Be half-life by multicollector ICP-MS and liquid scintillation counting. *Nuclear Instruments and Methods in Physics Research Section B: Beam Interactions with Materials and Atoms*, *268*(2), 192–199. https://doi.org/10.1016/j.nimb.2009.09.012

Densmore, A. L., Sinha, R., Sinha, S., Tandon, S. K., & Jain, V. (2015). Sediment storage and release from Himalayan piggyback basins and implications for downstream river morphology and evolution. *Basin Research*, *28*(4), 446–461. https://doi.org/10.1111/bre.12116

Dewald, A., Heinze, S., Jolie, J., Zilges, A., Dunai, T., Rethemeyer, J., et al. (2013). CologneAMS, a dedicated center for accelerator mass spectrometry in Germany. *Nuclear Instruments and Methods in Physics Research Section B: Beam Interactions with Materials and Atoms*, *294*, 18–23. https://doi.org/10.1016/j.nimb.2012.04.030

Dey, S., Thiede, R. C., Schildgen, T. F., Wittmann, H., Bookhagen, B., Scherler, D., & Strecker, M. R. (2016). Holocene internal shortening within the northwest sub-Himalaya: Out-of-sequence faulting of the Jwalamukhi thrust, India. *Tectonics*, *35*(11), 2677–2697. https://doi.org/10.1002/2015tc004002

Dingle, E. H., Sinclair, H. D., Attal, M., Milodowski, D. T., & Singh, V. (2016). Subsidence control on river morphology and grain size in the Ganga Plain. *American Journal of Science*, *316*(8), 778–812. https://doi.org/10.2475/08.2016.03

Dingle, E. H., Sinclair, H. D., Attal, M., Rodés, Á., & Singh, V. (2018). Temporal variability in detrital ^{10}Be concentrations in a large Himalayan catchment. *Earth Surface Dynamics*, *6*(3), 611–635. https://doi.org/10.5194/esurf-6-611-2018

Fülöp, R.-H., Codilean, A. T., Wilcken, K. M., Cohen, T. J., Fink, D., Smith, A. M., et al. (2020). Million-year lag times in a post-orogenic sediment conveyor. *Science Advances*, *6*(25), eaaz8845. https://doi.org/10.1126/sciadv.aaz8845

Gabet, E. J., Burbank, D. W., Pratt-Sitaula, B., Putkonen, J., & Bookhagen, B. (2008). Modern erosion rates in the high Himalayas of Nepal. *Earth and Planetary Science Letters*, *267*(3–4), 482–494. https://doi.org/10.1016/j.epsl.2007.11.059

Galy, V., France-Lanord, C., Beyssac, O., Faure, P., Kudrass, H., & Palhol, F. (2007). Efficient organic carbon burial in the Bengal fan sustained by the Himalayan erosional system. *Nature*, *450*(7168), 407–410. https://doi.org/10.1038/nature06273

Granger, D. E., Kirchner, J. W., & Finkel, R. (1996). Spatially averaged long-term erosion rates measured from in situ-produced cosmogenic nuclides in alluvial sediment. *The Journal of Geology*, *104*(3), 249–257. https://doi.org/10.1086/629823

Granger, D. E., & Riebe, C. S. (2014). Cosmogenic nuclides in weathering and erosion. In *Treatise on geochemistry* (pp. 401–436). Elsevier. https://doi.org/10.1016/b978-0-08-095975-7.00514-3

Hodges, K. V. (2000). Tectonics of the Himalaya and southern Tibet from two perspectives. *Geological Society of America Bulletin*, *112*(3), 324–350. https://doi.org/10.1130/0016-7606(2000)112⟨324:tothas⟩2.0.co;2

Hoth, S., Hoffmann-Rothe, A., & Kukowski, N. (2007). Frontal accretion: An internal clock for bivergent wedge deformation and surface uplift. *Journal of Geophysical Research*, *112*(B6), B06408. https://doi.org/10.1029/2006jb004357

Hu, X., Kirby, E., Pan, B., Granger, D. E., & Su, H. (2011). Cosmogenic burial ages reveal sediment reservoir dynamics along the Yellow River, China. *Geology*, *39*(9), 839–842. https://doi.org/10.1130/g32030.1

Hurtrez, J.-E., Lucazeau, F., Lavé, J., & Avouac, J.-P. (1999). Investigation of the relationships between basin morphology, tectonic uplift, and denudation from the study of an active fold belt in the Siwalik Hills, central Nepal. *Journal of Geophysical Research*, *104*(B6), 12779–12796. https://doi.org/10.1029/1998jb900098

Kirby, E., & Whipple, K. X. (2012). Expression of active tectonics in erosional landscapes. *Journal of Structural Geology*, *44*, 54–75. https://doi.org/10.1016/j.jsg.2012.07.009

Korschinek, G., Bergmaier, A., Faestermann, T., Gerstmann, U., Knie, K., Rugel, G., et al. (2010). A new value for the half-life of ^{10}Be by heavy-ion elastic recoil detection and liquid scintillation counting. *Nuclear Instruments and Methods in Physics Research Section B: Beam Interactions with Materials and Atoms*, *268*(2), 187–191. https://doi.org/10.1016/j.nimb.2009.09.020

Kumar, R., Ghosh, S. K., Mazari, R., & Sangode, S. (2003). Tectonic impact on the fluvial deposits of Plio-Pleistocene Himalayan foreland basin, India. *Sedimentary Geology*, *158*(3–4), 209–234. https://doi.org/10.1016/s0037-0738(02)00267-1

Kumar, R., Sangode, S. J., & Ghosh, S. K. (2004). A multistorey sandstone complex in the Himalayan foreland basin, NW Himalaya, India. *Journal of Asian Earth Sciences*, *23*(3), 407–426. https://doi.org/10.1016/s1367-9120(03)00176-7

Lal, D. (1991). Cosmic ray labeling of erosion surfaces: In situ nuclide production rates and erosion models. *Earth and Planetary Science Letters*, *104*(2–4), 424–439. https://doi.org/10.1016/0012-821x(91)90220-c

Lavé, J., & Avouac, J. P. (2000). Active folding of fluvial terraces across the Siwaliks Hills, Himalayas of central Nepal. *Journal of Geophysical Research*, *105*(B3), 5735–5770. https://doi.org/10.1029/1999jb900292

Lupker, M., Blard, P.-H., Lavé, J., France-Lanord, C., Leanni, L., Puchol, N., et al. (2012). ^{10}Be-derived Himalayan denudation rates and sediment budgets in the Ganga basin. *Earth and Planetary Science Letters*, *333–334*, 146–156. https://doi.org/10.1016/j.epsl.2012.04.020

Lupker, M., France-Lanord, C., Galy, V., Lavé, J., & Kudrass, H. (2013). Increasing chemical weathering in the Himalayan system since the last glacial maximum. *Earth and Planetary Science Letters*, *365*, 243–252. https://doi.org/10.1016/j.epsl.2013.01.038

Lyon-Caen, H., & Molnar, P. (1985). Gravity anomalies, flexure of the Indian Plate, and the structure, support and evolution of the Himalaya and Ganga Basin. *Tectonics*, *4*(6), 513–538. https://doi.org/10.1029/tc004i006p00513

Mandal, S. K., Kapannusch, R., Scherler, D., Barnes, J. B., Insel, N., & Densmore, A. L. (2023). *Cosmogenic ^{10}Be and ^{26}Al concentrations in fluvial sediments from the Mohand Range in the northwestern Himalaya*. GFZ Data Services. https://doi.org/10.5880/fidgeo.2023.027

Mandal, S. K., Scherler, D., Romer, R. L., Burg, J.-P., Guillong, M., & Schleicher, A. M. (2018). Multi-proxy isotopic and geochemical analysis of the Siwalik sediments in NW India: Implication for the late cenozoic tectonic evolution of the Himalaya. *Tectonics*, *38*(1), 120–143. https://doi.org/10.1029/2018tc005200

Mandal, S. K., Scherler, D., & Wittmann, H. (2021). Tectonic accretion controls erosional cyclicity in the Himalaya. *AGU Advances*, *2*(3), e2021AV000487. https://doi.org/10.1029/2021av000487

Miller, S. R., & Slingerland, R. L. (2006). Topographic advection on fault-bend folds: Inheritance of valley positions and the formation of wind gaps. *Geology*, *34*(9), 769. https://doi.org/10.1130/g22658.1

Milliman, J. D., & Farnsworth, K. L. (2011). *River discharge to the coastal ocean: A global synthesis*. Cambridge University Press. https://doi.org/10.1017/CBO9780511781247

Mishra, P., & Mukhopadhyay, D. K. (2002). Balanced structural models of Mohand and Santaurgarh ramp anticlines, Himalayan foreland fold-thrust belt, Dehra Dun re-entrant, Uttaranchal. *Journal of the Geological Society of India*, *60*(6), 649–661.

Mugnier, J.-L., & Huyghe, P. (2006). Ganges basin geometry records a pre-15 Ma isostatic rebound of Himalaya. *Geology*, *34*(6), 445–448. https://doi.org/10.1130/g22089.1

Najman, Y., Jenks, D., Godin, L., Boudagher-Fadel, M., Millar, I., Garzanti, E., et al. (2017). The Tethyan Himalayan detrital record shows that India–Asia terminal collision occurred by 54 Ma in the Western Himalaya. *Earth and Planetary Science Letters*, *459*, 301–310. https://doi.org/10.1016/j.epsl.2016.11.036

Najman, Y., Johnson, K., White, N., & Oliver, G. (2004). Evolution of the Himalayan foreland basin, NW India. *Basin Research*, *16*(1), 1–24. https://doi.org/10.1111/j.1365-2117.2004.00223.x

Niemi, N. A., Oskin, M., Burbank, D. W., Heimsath, A. M., & Gabet, E. J. (2005). Effects of bedrock landslides on cosmogenically determined erosion rates. *Earth and Planetary Science Letters*, *237*(3–4), 480–498. https://doi.org/10.1016/j.epsl.2005.07.009

Nishiizumi, K. (2004). Preparation of ^{26}Al AMS standards. *Nuclear Instruments and Methods in Physics Research Section B: Beam Interactions with Materials and Atoms*, *223–224*, 388–392. https://doi.org/10.1016/j.nimb.2004.04.075

Ori, G. G., & Friend, P. F. (1984). Sedimentary basins formed and carried piggyback on active thrust sheets. *Geology*, *12*(8), 475–478. https://doi.org/10.1130/0091-7613(1984)12⟨475:sbfacp⟩2.0.co;2

Phillips, F. M., Argento, D. C., Balco, G., Caffee, M. W., Clem, J., Dunai, T. J., et al. (2016). The CRONUS-Earth project: A synthesis. *Quaternary Geochronology*, *31*, 119–154. https://doi.org/10.1016/j.quageo.2015.09.006

Powers, P. M., Lillie, R. J., & Yeats, R. S. (1998). Structure and shortening of the Kangra and Dehra Dun reentrants, sub-Himalaya, India. *Geological Society of America Bulletin*, *110*(8), 1010–1027. https://doi.org/10.1130/0016-7606(1998)110⟨1010:sasotk⟩2.3.co;2

Sadler, P. M. (1981). Sediment accumulation rates and the completeness of stratigraphic sections. *The Journal of Geology*, *89*(5), 569–584. https://doi.org/10.1086/628623

Sadler, P. M., & Jerolmack, D. J. (2014). Scaling laws for aggradation, denudation and progradation rates: The case for time-scale invariance at sediment sources and sinks. *Geological Society, London, Special Publications*, *404*(1), 69–88. https://doi.org/10.1144/sp404.7

Sangode, S. J., Kumar, R., & Ghosh, S. K. (1996). Magnetic polarity stratigraphy of the Siwalik sequence of Haripur area (HP), NW Himalaya. *Journal of the Geological Society of India*, *47*, 683–704.

Sangode, S. J., Kumar, R., & Ghosh, S. K. (1999). Palaeomagnetic and rock magnetic perspectives on the post-collision continental sediments of the Himalaya, India. *Geological Society of India Memoir*, *44*, 221–248.

Sanyal, P., Bhattacharya, S., Kumar, R., Ghosh, S., & Sangode, S. (2004). Mio–Pliocene monsoonal record from Himalayan foreland basin (Indian Siwalik) and its relation to vegetational change. *Palaeogeography, Palaeoclimatology, Palaeoecology*, *205*(1–2), 23–41. https://doi.org/10.1016/j.palaeo.2003.11.013

Scherler, D., Bookhagen, B., & Strecker, M. R. (2014). Tectonic control on ^{10}Be-derived erosion rates in the Garhwal Himalaya, India. *Journal of Geophysical Research: Earth Surface*, *119*(2), 83–105. https://doi.org/10.1002/2013jf002955

Scherler, D., Bookhagen, B., Wulf, H., Preusser, F., & Strecker, M. R. (2015). Increased late Pleistocene erosion rates during fluvial aggradation in the Garhwal Himalaya, northern India. *Earth and Planetary Science Letters*, *428*, 255–266. https://doi.org/10.1016/j.epsl.2015.06.034

Small, E. E., Anderson, R. S., Repka, J. L., & Finkel, R. (1997). Erosion rates of alpine bedrock summit surfaces deduced from in situ ^{10}Be and ^{26}Al. *Earth and Planetary Science Letters*, *150*(3–4), 413–425. https://doi.org/10.1016/s0012-821x(97)00092-7

Srivastava, P., & Mitra, G. (1994). Thrust geometries and deep structure of the outer and lesser Himalaya, Kumaon and Garhwal (India): Implications for evolution of the Himalayan fold-and-thrust belt. *Tectonics*, *13*(1), 89–109. https://doi.org/10.1029/93tc01130

Srivastava, V., Mukul, M., Barnes, J. B., & Mukul, M. (2018). Geometry and kinematics of Main Frontal thrust-related fault propagation folding in the Mohand Range, northwest Himalaya. *Journal of Structural Geology*, *115*, 1–18. https://doi.org/10.1016/j.jsg.2018.06.022

Stevens, V. L., & Avouac, J. P. (2015). Interseismic coupling on the main Himalayan thrust. *Geophysical Research Letters*, *42*(14), 5828–5837. https://doi.org/10.1002/2015gl064845

Tadono, T., Nagai, H., Ishida, H., Oda, F., Naito, S., Minakawa, K., & Iwamoto, H. (2016). Generation of the 30 m-mesh global digital surface model by ALOS PRISM. *The International Archives of the Photogrammetry, Remote Sensing and Spatial Information Sciences*, *XLI-B4*, 157–162. https://doi.org/10.5194/isprs-archives-xli-b4-157-2016

Thakur, V., Pandey, A., & Suresh, N. (2007). Late Quaternary–Holocene evolution of Dun structure and the Himalayan frontal fault zone of the Garhwal sub-Himalaya, NW India. *Journal of Asian Earth Sciences*, *29*(2–3), 305–319. https://doi.org/10.1016/j.jseaes.2006.02.002

Vance, D., Bickle, M., Ivy-Ochs, S., & Kubik, P. W. (2003). Erosion and exhumation in the Himalaya from cosmogenic isotope inventories of river sediments. *Earth and Planetary Science Letters*, *206*(3–4), 273–288. https://doi.org/10.1016/s0012-821x(02)01102-0

van der Beek, P., Robert, X., Mugnier, J.-L., Bernet, M., Huyghe, P., & Labrin, E. (2006). Late Miocene - Recent exhumation of the central Himalaya and recycling in the foreland basin assessed by apatite fission-track thermochronology of Siwalik sediments, Nepal. *Basin Research*, *18*(4), 413–434. https://doi.org/10.1111/j.1365-2117.2006.00305.x

van Dijk, W. M., Densmore, A. L., Singh, A., Gupta, S., Sinha, R., Mason, P. J., et al. (2016). Linking the morphology of fluvial fan systems to aquifer stratigraphy in the Sutlej-Yamuna plain of northwest India. *Journal of Geophysical Research: Earth Surface*, *121*(2), 201–222. https://doi.org/10.1002/2015jf003720

von Blanckenburg, F., Belshaw, N., & O'Nions, R. (1996). Separation of ^{9}Be and cosmogenic ^{10}Be from environmental materials and SIMS isotope dilution analysis. *Chemical Geology*, *129*(1–2), 93–99. https://doi.org/10.1016/0009-2541(95)00157-3

Webb, A. A. G., Yin, A., Harrison, T. M., Célérier, J., Gehrels, G. E., Manning, C. E., & Grove, M. (2011). Cenozoic tectonic history of the Himachal Himalaya (northwestern India) and its constraints on the formation mechanism of the Himalayan orogen. *Geosphere*, *7*(4), 1013–1061. https://doi.org/10.1130/GES00627.1

Wesnousky, S. G., Kumar, S., Mohindra, R., & Thakur, V. C. (1999). Uplift and convergence along the Himalayan frontal thrust of India. *Tectonics*, *18*(6), 967–976. https://doi.org/10.1029/1999tc900026

Wittmann, H., Oelze, M., Gaillardet, J., Garzanti, E., & von Blanckenburg, F. (2020). A global rate of denudation from cosmogenic nuclides in the Earth's largest rivers. *Earth-Science Reviews*, *204*, 103147. https://doi.org/10.1016/j.earscirev.2020.103147

Wittmann, H., von Blanckenburg, F., Guyot, J., Maurice, L., & Kubik, P. (2009). From source to sink: Preserving the cosmogenic ^{10}Be-derived denudation rate signal of the Bolivian Andes in sediment of the Beni and Mamoré foreland basins. *Earth and Planetary Science Letters*, *288*(3–4), 463–474. https://doi.org/10.1016/j.epsl.2009.10.008

Yin, A., & Harrison, T. M. (2000). Geologic evolution of the Himalayan-Tibetan Orogen. *Annual Review of Earth and Planetary Sciences*, *28*(1), 211–280. https://doi.org/10.1146/annurev.earth.28.1.211